Universidad Nacional Autónoma de México

Facultad de Ciencias

Characterization of the time response of a monolithic silicon pixel detector using a pulsed IR laser

T E S I S

que para obtener el título de:

Licenciado en Física

presenta:

Andrea Pizarro Medina

Tutor:

Prof. Giuseppe Iacobucci

Co-tutor:

Prof. Lorenzo Paolozzi

CDMX, México 2021

A mis padres, maestros y amigos, cuyo apoyo ha sido esencial para culminar este trabajo.

Acknowledgments

In this small section I would like to make a special mention the all the people who impacted on this work, and without whom it would not have been possible.

First of all, I need to thank Prof. Giuseppe Iacobucci, who generously opened the doors of his research group to me, gave me trust and support since the beginning, and for that I will be forever grateful.

I also want to thank Prof. Lorenzo Paolozzi for being a guide to this work, for daily sharing his extensive knowledge, and for always being willing to answer questions and get involved in enriching discussions.

I am grateful to my fellow students and co-workers at UNIGE, with whom I shared valuable experiences and learnings during the process of carrying out this work.

Last but not least, I thank all the teachers who were my professors at UNAM, who laid the foundations of my knowledge and my professional training, which made it possible for this work to be successfully completed.

Abstract

The importance of developing timing detectors with few picoseconds time resolution has become evident in the past decades, due to the growing need for better time and spatial resolution by the sectors of High Energy Physics (HEP), Medical Physics, fine 2D and 3D imaging, ranging, among others.

The work summarized in this Thesis consisted of the characterization of the time response of a monolithic silicon detector with high performance integrated electronics based on SiGe BiCMOS technology.

Numerous bibliography supports the fact that such technology is capable of improving the time resolution of detectors to less than 100 ps, without the need to use a gain layer or an avalanche gain mechanism such as the one implemented in a Low-Gain Avalance Diode (LGAD), which is used as a reference timing detector due to its excellent and well-documented response.

The alternative of timing detectors based on a SiGe BiCMOS technology applied in monolithic detectors represents several advantages. Monolithic detectors, compared to typical hybrid detectors which are very popular on the market, are thinner, cheaper, and with a robust composition. This is the reason why they represent an important R&D opportunity. This work confirmed that a sensor based on this technology achieves time resolutions below 20ps, and by implementing a gain layer on such a sensor, the temporal resolution can be brought below 10ps, both considering a high power consumption budget.

Contents

CHAPTER 1

Introduction

1.1 Timing particle detectors

In present times, the importance of technology for research and development of basic and applied science has become more clear than ever. In the past few decades, a lot of resources have been invested in the research for new and better technologies in the field of High Energy Physics. Amazing achievements have been made, among which we can point out the discovery of the Higgs boson [1], the description of the nature of neutrinos [2], or the better understanding of antimatter [3]. However, the experiments that are carried out to continue progressing in this field, have become incredibly complex and require more precision to be able to resolve phenomena that are increasingly imperceptible to the present instrumentation.

That is why, in addition to investing efforts in the study and development of theoretical physics, it is extremely important to provide intellectual resources to experimental physics projects in order to improve the technology that is currently available. Moreover, aside from the value that it has for the scientific community, experimental and applied physics have the potential to produce significant benefits for the society in the short term.

This particular work will focus on the development of ultra-fast particle detectors. The ultra-fast time resolution then translates into better spatial resolution in time-of-flight (TOF) measurements, as well as a more accurate reproduction of the trajectories of the particles that reach the detector.

In our case, we must analyze the history and evolution of solid state detectors and how these have been chosen as good candidates for many different applications such as high energy particle detectors at CERN, but also medical imaging, radars, satellite communications, instrumentation, among many other areas that take advantage of the development of semiconductor technologies.

At the end of the 19th century, semiconductors were discovered, ushering in an era of developments of electronics, allowing the development of ever smaller and faster devices, leading to the modern microelectronics that we have today [4]. Everyday life devices such as computers, mobile phones, internet, as well as ever smarter cars, home appliances, among others, have been only possible thanks to the development of microelectronics based on silicon transistors. At the same time, this technology allowed the emergence of faster and more accurate sensors used in the field of experimental physics. In the following, the importance of the development of timing detectors in High Energy Physics as well as in the field of Medical Physics will be discussed.

1.2 High Energy Physics Applications

Without a doubt, the reference in terms of High Energy Physics (HEP) research, due to its magnitude and its consolidated results over the years, is the scientific research carried out at the European Center for Nuclear Research (CERN by its acronym in French), and above all, the experiments carried out at the Large Hadron Collider (LHC). Due to the size of these experiments, and the amount of data that is generated daily, data processing capabilities have to be efficient to meet the statistical and resolution standards necessary for the publication of results. It is for this reason that a tracking detector that can improve time resolution to an order of at least hundreds of picoseconds represents a growing need, especially taking into account CERN's future projects.

To illustrate the importance of improving time resolution in HEP experiments, we can mention the case of ATLAS experiment and its design and timing properties. A $50\mu m \times 250\mu m$ rectangular silicon pixel detector system for the innermost layer (IBL) has been implemented in the LHC ATLAS experiment to obtain better spatial resolution in one of

the two directions [5]. At the moment, the pixel detector has a time resolution of 25 ns [6]. However, when we find a high density of particles reaching the detector, there is the possibility of having more than one event per strip, giving rise to what is known as *pile-up*, which is the ambiguity of having so many collision events in such a short amount of time, that is impossible to resolve every single vertex, resulting in two (or more) events detected as one. Pile-up can be reduced when the detector's time resolution improves, therefore, improving the trajectory reconstruction capability of the experiment.

Figure 1.1 shows the reconstructed trajectories of secondary particles produced in a Pb-Pb collision at the ALICE experiment in 2011 [7]. This figure gives an idea of the density of secondary particles whose trajectories are represented in different colors. Similarly, in Figure 1.2 we can appreciate how the pile-up phenomenon is an issue if the detectors do not have sufficient time resolution [8]. We can see that 25 vertices have been resolved, showing its secondary particle trajectories in different colors for different vertices. The two thick yellow lines correspond to a dimuon decay, whereby it has been identified as a candidate for the Z-boson particle.

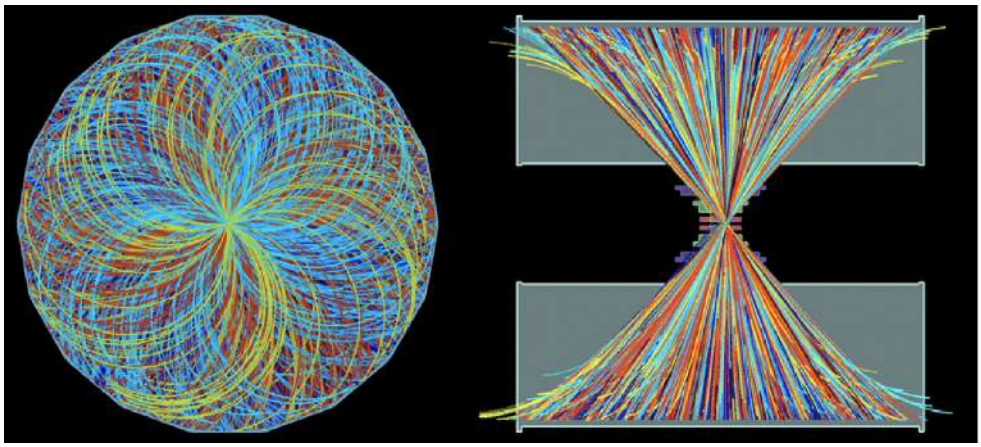

Figure 1.1: Trajectory of secondary particles in a Pb-Pb event. Alice, 2011 [7].

Let us consider the present experiments at the LHC at a beam luminosity of $10^{34}\text{cm}^{-2}\text{s}^{-1}$, where bunches of 100 billion particles are collided with a frequency of 40 MHz. Under these conditions, each time two bunches intersect, which happens every ~ 25 ns, between $40-50$ collisions between particles traveling in opposite directions are generated [5]. If the High Luminosity LHC (HL-LHC) experiments are considered, the number of collisions increases

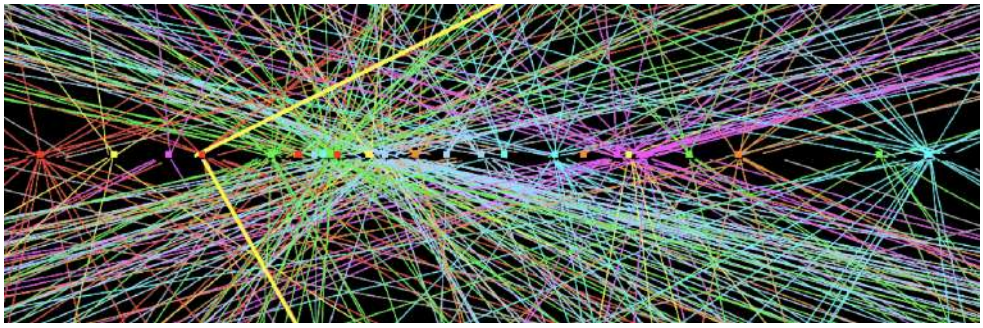

Figure 1.2: Z-boson candidate event in a dimuon decay with 25 reconstructed vertices; illustration of the pile-up phenomenon. ATLAS, 2012 [8].

to $400 - 500$ per bunch crossing [9]. These collisions give rise to, what is called, a *vertex* from which secondary particles emerge from the collision. Then it is then necessary to recreate the trajectory of the particles produced in each collision. Note that given a frequency of 40 MHz, there are 40 million bunch crossings per second, which implies about 2 billion collisions per second that generate secondary particles. There is no doubt that analyzing this amount of data is highly impractical and even unfeasible for today's best supercomputers. To reduce the number of events that are stored for later analysis, there are several stages of selection. The first stage consists mostly of the use of FPGA or TPD hardware systems [10]. The second stage involves an analysis applying threshold cuts to low energy particles among other events that are not relevant.

Having detectors with a time resolution of the order of 100 picoseconds or better, will reduce pile-up ambiguities, so that the trajectories to each vertex can be traced with greater precision and reliability [11]. Since the area to cover in a pixel detector such as LHC ATLAS is of the order of 100 m^2, it is extremely important to be able to minimize the power consumption. Hence, it is not only important to improve the time resolution of the detector, but also doing it within a limited power consumption budget. For fast pixel tracking detectors, this would mean to keep a good time resolution below 100 ps at the same time that the power consumption of an order of $100 mW/cm^2$.

1.3 Medical applications

It is also worth mentioning the medical applications in which this work is relevant. In recent decades, special emphasis has been placed on the development of nuclear medicine as a novel treatment and an advanced imaging method for cancer and other diseases. This is the case with Positron Emission Tomography (PET) [12]. This imaging technique consists of administering a radiopharmaceutical that contains a small amount of a radioactive isotope normally produced in a cyclotron, such as ^{11}C, ^{13}N, ^{15}O or ^{18}F. The isotopes are created in a cyclotron instead of a linear accelerator or other methods due to its versatility. The energy range at which the cyclotron is operated is typically of $10 - 20$ MeV [13].
The production of the radionuclides can be through two processes: either neutrons or charged particles as irradiation source. Neutron irradiation leads to neutron capture reaction, and thus, neutron-enriched nuclei. Charged particle irradiation leads to a reaction of the form (p,xn) or (p,α), and therefore results in neutron-deficient nuclei. The radionuclides can be administered to patients intravenously through a special saccharide composition, such as the [^{18}F]-fluorodeoxyglucose. Subsequently, tissues with high consumption, such as cancerous tumors, concentrate the radiopharmaceutical and emit higher levels of radiation. These radioactive sources inside the body therefore emit positrons via $\beta+$ radioactive decay, which, in contact with surrounding electrons, give rise to a particle-antiparticle annihilation and the production of a pair of photons. The resulting interaction is as follows:

$$e^+ + e^- \rightarrow \gamma + \gamma$$

In the previous reaction, both energy and momentum must be conserved. Due to moment conservation, the photons are emitted back-to-back, generating a line-of-response. This is how, for example, cancerous tumors can be identified by detecting the light that is emitted from electron-positron annihilation. This γ radiation then reaches the detector and produces an image such that, together with results obtained from a nuclear magnetic resonance, a mapping of the structure and the precise location of the tissue of interest

is achieved. In Figure 1.3, a simplified diagram of the process of positron emission from the radionuclide, anihilation with an electron, and further production of two back-to-back gamma rays that are detected in the PET Scanner.

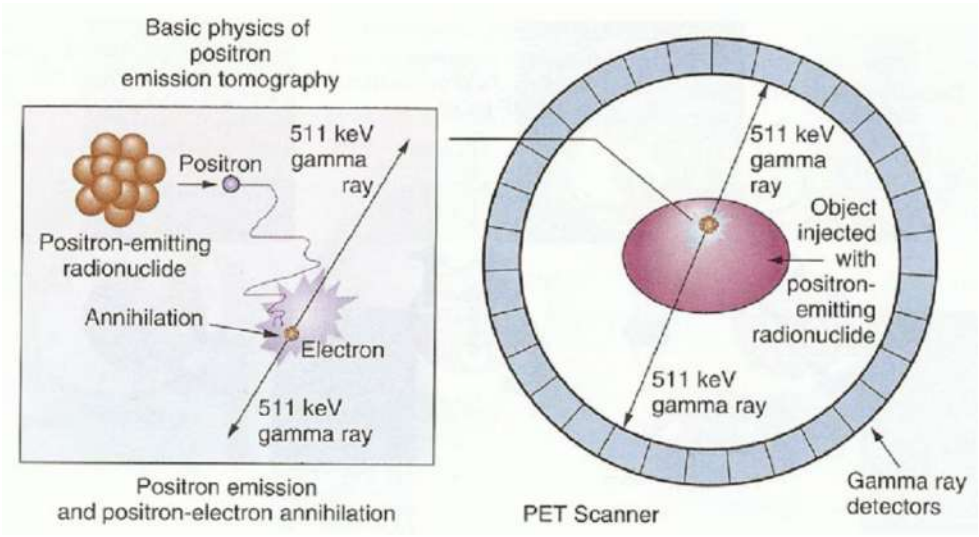

Figure 1.3: Photon detection by electron-positron annihilation principle used at PET scanners [14].

The importance of developing a detector that significantly reduces its time resolution to the order of picoseconds means, in this context, identifying the position of the $\beta+$ emission along each line-of-response, thus locating the malignant tissue with a precision of the order of millimeters. This then translates into more efficient clinical examinations, the ability to use better focused treatments and avoiding long and unnecessary exposure of patients to high doses of radiation.

CHAPTER 2

Timing detector development

2.1 Bethe-Bloch Equation

In order to detect a particle, such particle must have an interaction with the material and transfer energy into it in a way that can be measured. That's why it is important to understand the processes of energy transfer between the radiation that comes in the detector, and the matter inside the detector itself.

For charged particles such those coming from β radioactive sources majorly undergo an electromagnetic interaction with its medium which gives place to excitation and ionization of the medium. If the medium itself is kept under a difference of potential, the charges generated after ionization will give rise to a detectable signal. The basic principle of interaction of charged particles with matter and how the particles transfer their energy is best modeled by the Bethe-Bloch equation [15].

The derivation of Bethe-Bloch equation considers an incoming charged particle with mass greater than that of the electron mass and it presumes mostly elastic collisions with the electrons of the medium. These assumptions result in the following expression:

$$\frac{dE}{dx} = \frac{4\pi n Z^2 e^4}{m_e v^2}\left[ln\left(\frac{2m_e\gamma^2 v^2}{I(1-\beta^2)}\right) - \beta^2 - \frac{\delta}{2}\right] \tag{2.1}$$

where n is the electronic density of the medium, Ze is the charge of the incoming particle, v is its speed, γ is the Lorentz Factor $\gamma = 1/\sqrt{1-\beta^2}$ and $\beta = v/c$, and the $\delta/2$ term is

the correction for the effect of saturation of charge, which needs to be taken into account for high energy interactions. The parameter I is called the *ionization constant* and it encompasses the atomic characteristics of the medium regarding the excitation / ionization properties. This constant has been measured experimentally, and in practical terms we can assign its value as a function of Z with the following relation:

$$\frac{I}{Z} = \begin{cases} 12 + \frac{7}{Z} & [eV];\ Z < 13 \\ 9.76 + 58.8Z^{-1.19} & [eV];\ Z \geq 13 \end{cases}$$

The Bethe-Bloch Equation describes the stopping power of a heavy charged particle in a material. In the case of electrons and/or positrons, this equation must be corrected for radiative losses, which are considerable for light particles. However, under certain conditions, it is still possible to model the behaviour of β particles inside a thin silicon detector with the Bethe-Bloch equation [16]. Note that, for relativistic particles where $\beta\gamma \approx 3$, the energy loss per unit length reaches a minimum, therefore called the minimum ionization regime. A particle that belongs in the minimum ionizing regime, is hence defined as a Minimum Ionizing Particle (MIP). The stopping power of a MIP is easy to compute, and a good approximation for relativistic β particles in a thin silicon detector. Therefore, if β radiation can be approximated as a source of MIPs, its energy deposition in the detector's material should follow a Landau distribution which can be parameterized in terms of λ by the following expression:

$$L(\lambda) = \frac{1}{\sqrt{2\pi}} e^{-\frac{\lambda + e^{-\lambda}}{2}} \tag{2.2}$$

where $\lambda = (\Delta E - \Delta E_W)/\xi$ is the difference between the energy loss in the medium of thickness Δx and the most probable value of energy loss for that same medium thickness. The parameter ξ determines the width of the distribution.

2.2 Photoelectric Effect

If we now consider not charged particles but incoming photons into a solid-state particle detector, there are basically four processes that might occur as the photons interact with the medium [15]:

- Photoelectric effect
- Rayleigh diffusion
- Compton diffusion
- Pair production e^+e^-

For the effects of the matter that concerns us, we will only discuss the photoelectric effect as the other processes do not signify considerable effects in thin silicon detectors.
The photoelectric effect was predicted by A. Einstein in 1905 [17] after several decades of work on electromagnetism, optics and the early stages of quantum mechanics. This effect arises from the idea that light existed in a discrete number of packs, or *quanta* of energy. This discretization enforced the concept of a light particle, or photon, that could exchange energy with the electrons of a material. To illustrate the photoelectric effect, we must consider the layer model of the atom, in which outer layer electron will be weaker to pull off of the nuclear potential, and inner layer electrons will require a more energetic "kick" to be detached.
Let us consider an electron attached to its nucleus with a certain amount of binding energy E_B. If a photon with an energy E_γ collides with and is absorbed by the electron, it has now sufficient energy to be pulled off the nuclear potential and to have a net kinetic energy as a free electron. The ejected electron can be now called *photoelectron*. This process is represented by the following expression:

$$\gamma + e^- \rightarrow e^- + \text{X-ray}, \tag{2.3}$$

and the balance of energy between photon and electron can be written as:

$$E_{e^-} = E_\gamma - E_B \tag{2.4}$$

where $E_\gamma > E_B$ in order for the process to be feasible.
This effect is dominant as long as $E_\gamma < 100$ KeV, and if we consider a, IR laser source of wavelength $\lambda = 1060$ nm, the energy of the photons emitted can be calculated as

$$E_\gamma = \frac{hc}{\lambda} = \frac{1240 \text{ eV} \cdot \text{ nm}}{1060 \text{ nm}} = 1.1698 \text{ eV}$$

Then, after the photoelectron has been detached from its atomic orbital, it leaves behind a hole that will be quickly filled by another electron from a higher energy level. Thus, the jump from a higher to a lower energy level will produce the emission of an X-ray of energy ΔE, the difference of potential energy from the higher to the lower state.
This is the process that dominates when incoming IR laser radiation comes into a silicon particle detector of 30 μm of thickness.

2.3 Detection process on pixel detectors

There are determining factors that distinguish the design of a particle detector, such as the nature of the particle to be detected, the range of energy that the detected particle can have, the kinematics of the particle inside and outside the detector, the physical process that occurs inside of the detector, and the size of the detector.
The detector that concerns this work, has the particular characteristic of being a monolithic silicon pixel sensor that was characterized under three different sources of radiation. $\beta-$ particles emitted by a ^{90}Sr radioactive source, X-rays from a ^{109}Cd source, and on the other hand, photons coming from an IR laser source. Let us consider the main process that describes the transfer of energy between a β particle emitted by a radioactive source such as ^{90}Sr, and the detector itself. This is the ionization process that obeys the Bethe-Bloch equation. On the other hand, in the case of an X-ray or laser source, where the radiation in question are photons, the ionization of the material inside the sensor occurs

due to the photoelectric effect.

In order to reduce the number of variables that introduce noise into the system, and to simplify as much as possible the design of the detector and the model that describes it, some key considerations were made. Considering a silicon monolithic pixel detector with a thickness of ~ 100 μm, the time that it takes for the particle to pass through the detector, generate free charges within it and create a signal, is less than 1 ps. Also considering that the particle is travelling at relativistic speed, the following points can be considered as negligible:

- the particle's speed
- the size of the detector
- the detection process

This approximation can be done because the sensor is thin enough, such that the process inside it is independent of the trajectory of the particle before reaching the detector. Also, the fact that we are talking about a pixel detector, means that it is not the size of it that is important, but the size of the pixel with respect to the thickness. Therefore, the geometry has to be taken into account, not in the overall size of the detector, but the relation between the pixel size vs. detector thickness. This along with the fact that we are treating with a monolithic detector, allows it to be smaller and more compact, and still achieve outstanding results.

Now we must consider, in addition to the sensor itself, the electronic system that reads the signal generated within the sensor. The electronic reading system is in charge of translating the signal produced within the sensor, processing it, and sending it to the measurement instruments.

For a pixel particle detector, we can concentrate on 3 main characteristics:

1. Geometry of the readout
2. Charge collection noise
3. Electronic noise

These properties can be described quantitatively with the help of the Schockley-Ramo Theorem.

2.3.1 Shockley-Ramo Theorem

The *Shockley-Ramo Theorem* describes the current that is induced by moving charges in a system of electrodes kept at a fixed potential. This theorem was the result of the research work of William Shockley and Simon Ramo in 1938 [18] and 1939 [19], respectively, which is summarized in the following equation:

$$I_{ind}(t) = \sum_i q_i(t) \cdot \vec{E}_W(\vec{x_i}) \cdot \vec{v}_{d,i}(\vec{x_i}) \tag{2.5}$$

where $I_{ind}(t)$ is the induced current in the electrode, q_i is the i_{th} charge generated inside the detector, which can be positive or negative, *i.e.* for a semiconductor, a hole or an electron. $\vec{E}_W(\vec{x_i})$ is called the *weighting field* and it can be computed as the electric field that would be generated by keeping the target electrode at a difference of potential of 1V, and the rest to ground (0V). Finally, $\vec{v}_{d,i}(\vec{x_i})$ is the drift velocity of the charges generated within the detector.

Considering a detector with wide pixels with respect to the thickness of its depletion region, we can approximate the field inside the detector as the one generated in a parallel plate capacitor, and the Schockley-Ramo Theorem remains useful to model the current induced by the moving charges in the silicon material of the sensor.

In this configuration, it is possible to achieve the following characteristics:

- a uniform weighting field
- a uniform electric field
- reach the saturation of the drift velocity of the charge carriers

The production of charge inside a silicon detector can be pictured as in the diagram shown in Figure 2.1.

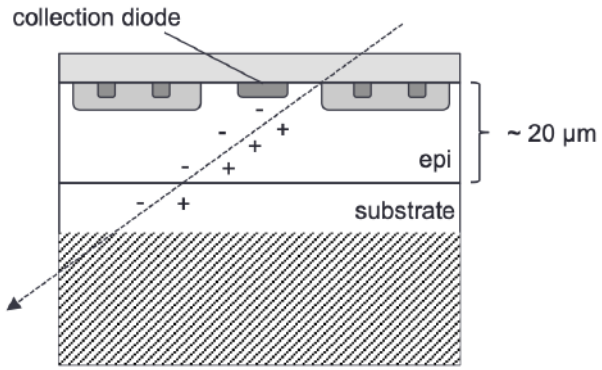

Figure 2.1: Charge production diagram within a monolithic semiconductor detector [7].

Note that, if the pixels are wide with respect to the thickness of the detector, the relationship between the drift velocity $\vec{v}_d$ and the electric field $\vec{E}$ (which can be compared to the weighting field) has a behavior like the one in Figure 2.2.

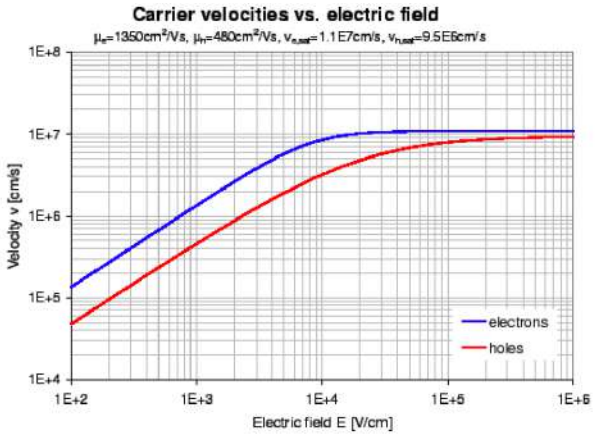

Figure 2.2: Drift velocity vs. electric field reached by electrons and holes (carriers) inside silicon [20].

It is desired that the carriers in the detector reach a saturated drift velocity, as this allows the detector to perform in optimal conditions regarding speed and uniformity of response [16].

In the wide pixel approximation we can simplify Equation 2.5 as follows:

$$I_{ind}(t) \simeq \frac{v_{s,d}}{D} \sum_i q_i(t), \tag{2.6}$$

where D is the depletion layer of the detector, which depends on its composition and geometry.

Now, for silicon, the saturation field $E_{sat} \sim 2-3$ V / μ m ($2-3\times10^4$ V / cm). Therefore, if using small pixels with respect to thickness, pulses had been observed as shown in Figure 2.3(a), when using large pixels we will obtain something as shown in Figure 2.3(b). If the detector is not fully depleted, saturation drift velocity is not reached by the charge carriers, and the quality of response is lower in terms of fast timing and linearity.

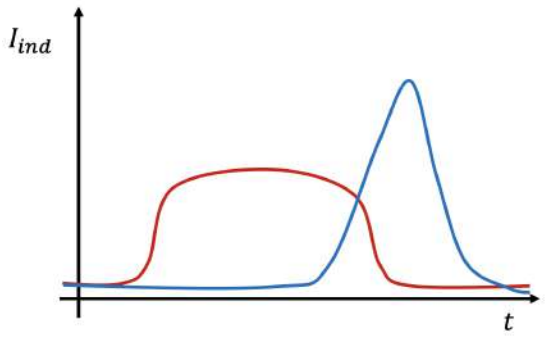

(a) Shape of pulses produced in detectors with small pixels with respect to D. In red, the shape of a pulse where the charge collection is slower and approximately constant over time. In blue, a pulse is shown where most of the charge is collected towards the end of the signal. In both cases, the timing characteristics of the signal are not ideal.

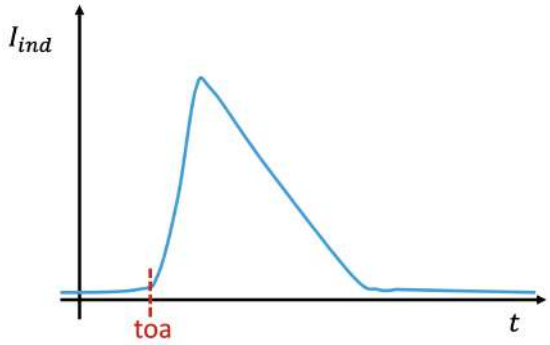

(b) Shape of pulses produced in detectors with large pixels with respect to D.

Figure 2.3: Comparison of the shape of the pulses obtained with small pixel detectors vs. large pixels (relative to thickness). The pulses show the integral of the charge collected with respect to time.

However, charge collection noise is a present phenomenon and must be taken into account. This is associated to the different size of the charge clusters produced by the primary ionization that are collected over time, so instead of observing a pulse like the one in Figure 2.3(b), we will actually have one similar to the one in Figure 2.4.

Since the time jitter associated to charge collection noise is < 10 ps for a 30 μm thin

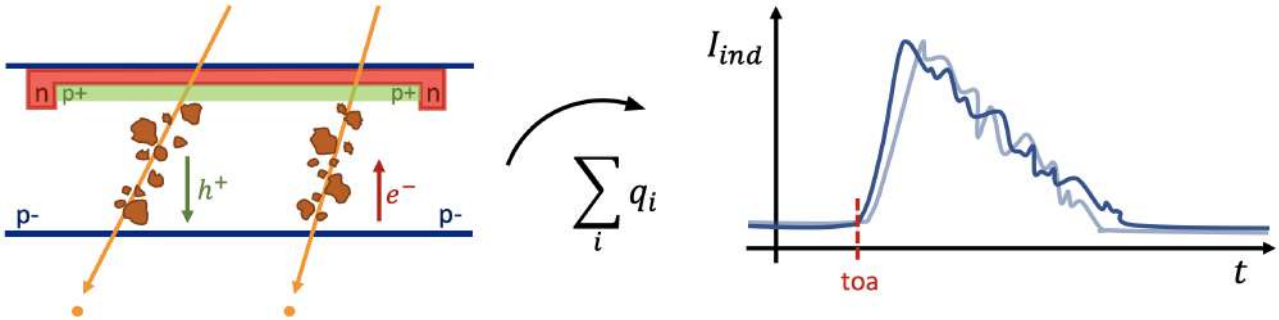

Figure 2.4: Charge collection noise due to charge clusters of different sizes arriving to the surface of the detector.

detector, this represents the physical limit of time resolution for this type of detectors. Therefore, this project seeks to get as close as possible to this value.

The last contribution to the time resolution of a particle detector is the noise introduced due to electronic signal reading systems. Returning to Equation 2.6, note that each term represents the factors of interest mentioned above:

$$\underbrace{I_{ind}(t)}_{\substack{\text{measurement}\\(\text{electronics})}} \simeq \overbrace{\frac{v_{s,d}}{D}}^{\text{geometry}} \underbrace{\sum_i q_i(t)}_{\substack{\text{charge}\\\text{collection}\\\text{noise}}}, \tag{2.7}$$

After considering the geometry and the charge collection noise, it remains for us to consider the contribution from the amplifier (and therefore the electronics that are involved with it) to the time resolution. This means that we are looking to minimize the noise originated from the charge amplifier.

At this point, we need to introduce the concept of *Equivalent Noise Charge*, or *ENC*. This quantity allows to separate the different sources of noise and translate each contribution into charge units $[e^-]$ referred to the input of the charge amplifier.

The electronic noise has two different sources, which are the equivalent noise voltage and the equivalent noise current. The expression for ENC contemplates the current noise (parallel), the voltage noise (series), and the $1/f$ voltage noise (or Flicker noise) [21]. The voltage noise is the one to take into consideration to determine the performance of a fast

amplifier and its contribution to the time resolution [22].
Let us consider the expression for ENC as follows:

$$ENC^2 = ENC^2_{series} \cdot \frac{1}{\tau_M} + ENC^2_{parallel} \cdot \tau_M + ENC^2_{1/f} \tag{2.8}$$

where τ_M is the integration time.

Now, we shall consider that for a fast charge integrator based on Bipolar Junction Transistors (BJT),

$$ENC_{series} \propto \sqrt{a \cdot R_B + \frac{b}{\beta}} \tag{2.9}$$

and the objective is to minimize ENC_{series}. In the amplifier circuit under study, R_B stands for the base resistance, and β is the current gain. For NPN BJTs, the latter can be expressed in terms of the currents of the collector and the base or of the average recombination/transit times inside the transistor. Thus,

$$\beta = \frac{I_C}{I_B} = \frac{\langle \tau_{recomb} \rangle}{\langle \tau_{transit} \rangle}$$

Hence, in order to minimize ENC_{series} and, with it, the time resolution of the amplifier, we must increase β maintaining a low R_B. For this aim, the Silicon-Germanium Heterojunction Bipolar Transistors (SiGe HBTs) technology was looked upon as a great option to increase β while reducing the dimensions of the sensor.
The SiGe HBT is an important accomplishment of solid-state engineering, and heritage of the work done in transistor development by Shockley in 1956. This technology is based on the working principle of the BJT, but implementing a grading of the bandgap in the Base using Germanium integrated into the silicon, which elongates the crystalline structure along one direction, generating a drift of charges from base to collector instead of transporting them only by diffusion as in a classic BJT. This mechanism of field-assisted charge transport, allows to establish a net direction of the current and lower times of transit $\tau_{transit}$. Therefore β is considerable increased. As a consequence of the directional drift of charges achieved in SiGe HBTs, the size of the detector can be reduced without

compromising the gain level β, and as a result of the decreased geometry, R_B will also drop, which translates into a better performing amplifier with faster responses and low-noise signals.

2.4 Design and characteristics of the sensor

For the past few years, monolithic silicon pixel detectors have started to be considered as a good alternative to hybrid detector for many reasons. So much so, that even some major high-energy physics experiments have already transitioned to monolithic detectors as a better and more affordable option, at the same time that time resolution, power consumption and radiation tolerance requirements are met [7]. Three of these LHC experiments are shown in Figure 2.5. To understand better the reasons for the investment in

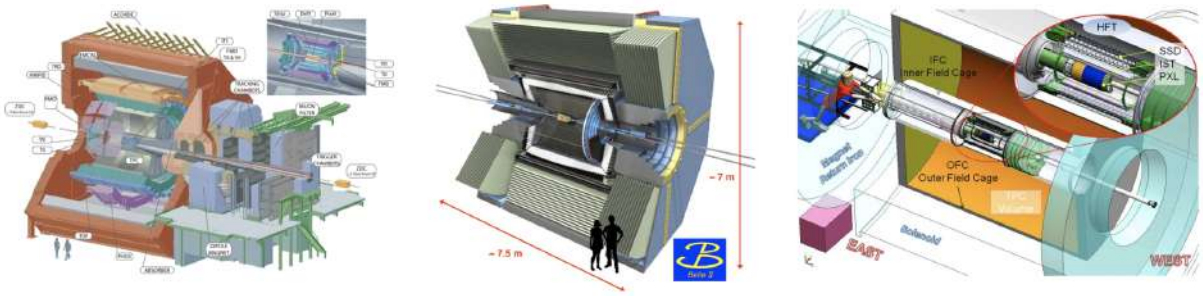

Figure 2.5: Examples of different HEP experiments that have chosen to evolve to monolithic detectors. From left to right, ALICE, BELLE II, STAR [7].

monolithic pixel detectors, we shall consider the main differences between a typical hybrid pixel detector and a monolithic detector.

In general, hybrid pixel sensors have a coupled structure where the electronics for the readout are superimposed on the sensor, so that each pixel has to be soldered to the electronic board. This type of detector has some advantages and certainly other disadvantages:

Advantages:

- independence between electronics and sensor
- use of distinct materials in the sensor
- flexibility

Disadvantages:

- cost
- thickness
- brittleness at weld points

The alternative to this type of sensor is the monolithic detector, which consists of a compact detector that integrates the electronics in the same silicon substrate of the chip. In Figure 2.6 we can appreciate the main difference between a typical hybrid sensor (Figure 2.6(a)), and a monolithic sensor (Figure 2.6(b)).

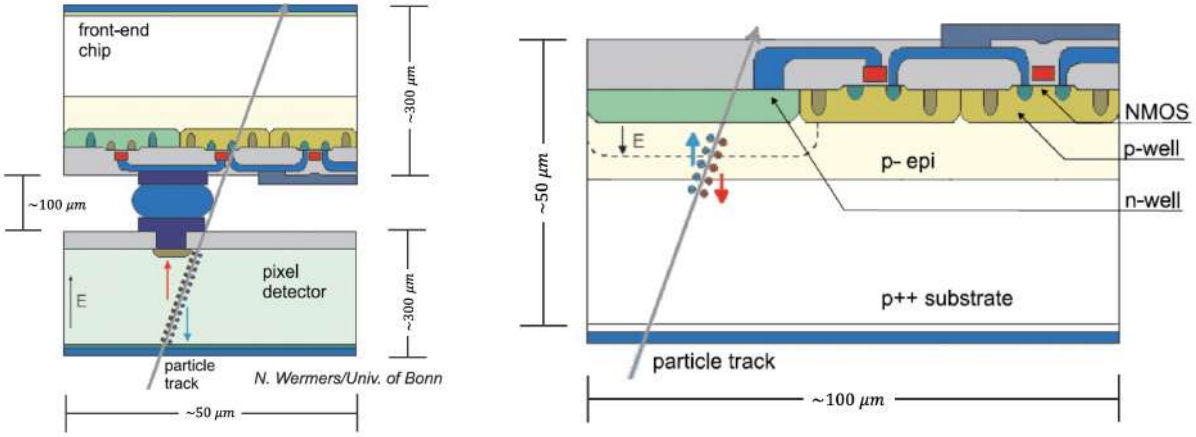

(a) Hybrid sensor

(b) Monolith sensor

Figure 2.6: Example of a typical hybrid detector vs. a monolithic detector [7].

The process used for the monolithic silicon detector investigated for this work is SiGe Bipolar Complementary Metal-Oxide-Semiconductor (BiCMOS).

Note that, in a typical hybrid detector, the characteristic resistivity of the substrate is of $\rho \sim 5000\ \Omega\cdot\text{cm}$, while in a detector such as the one being discussed, because of its considerable smaller geometry with respect to the hybrid detector, the substrate resistivity can go as low as $\rho \sim 50\ \Omega\cdot\text{cm}$. Considering then the expression:

$$W \propto k\sqrt{V}, \tag{2.10}$$

we note that the geometry and resistivity of the detector are decisive in calculating

the difference of potential generated within the detector. This implies that, by reducing the resistivity of the substrate used for the production of the detector, it is possible to considerably reduce the dimensions of the detector. The detector substrate used in this work has a resistivity of $\rho = 50\ \Omega\cdot$cm due to the specifications of the manufacturers, however, it is intended that in the future, a resistivity of $\rho = 200/300\ \Omega\cdot$cm can be used on the sensor substrate.

2.5 Expected time resolution vs. previous references

Since the objective of this project is help the development of an ultra-fast detector with time resolution of the order of picoseconds, we must take a look at an established reference accepted as the standard of time performance for ultra-fast timing.

An LGAD (Low-Gain Avalance Diode) is a silicon sensor that has been developed from the needs that have arisen, mainly, in High Energy Physics experiments. Specifically, the ATLAS and CMS experiments have had to invest in the research of LGADs to address the *pile-up* problem, especially in the HL-LHC (High-Luminosity Large Hadron Collider) project [23].

In theory, an LGAD detector can reach a time resolution of down to 20 ps [23], which is an outstanding time resolution in the HEP context.

The aim of this work will be to verify that monolithic silicon pixel sensors in SiGe BiCMOS can achieve a time resolution comparable with those of the LGAD but without the need of an avalanche gain mechanism [24].

2.6 The ATTRACT project chip prototype

The chip design of the prototype that was used throughout this work, was done by PhD. Lorenzo Paolozzi and PhD. Pierpaolo Valerio under the direction of Prof. Giuseppe Iacobucci at the University of Geneva. The design of this prototype represents a proposal for an ultra-fast particle detector that can achieve a time resolution of a few picoseconds. Its design and characterization were part of a one-year project for the development of a

proof-of-concept of timing detectors financed by the phase-I ATTRACT European support program for the development of innovative technologies. Therefore, it will be common to refer to this design as the ATTRACT prototype.

The ATTRACT prototype is made up of a monolithic silicon chip with a matrix of hexagonal pixels, of which only 4 are intended for analog channels and are therefore of interest to us. The chip design can be appreciated in Figure 2.7.

The production of the chips is carried out in multiple copies of the same reticle using a single wafer. However, even if each chip has exactly the same design and its manufacturing is carried out with the same process, it is possible that some of the chips coming from different reticles show significant mismatch variations, especially if the design or the process is novel, in which case they are more prone to be defective. Once the batch of chips is ready and comes out of the foundry, it is standard to do a first test on the chips at the probe station. This allows making a direct current (DC) characterization of the chip and see if their operation is correct, to identify the breaking points when applying voltages and currents in the detector, and determining if the behavior is close, or not, to the theoretical expectation and previous simulations. DC characterization is faster and easier than alternating current (AC) frequency testing, and it is good as a preliminary characterization of a new prototype. This test typically consists on plotting of the I-V curves of the chip under high-voltage biasing.

Once having satisfactory results from the DC test, the chip is wire-bonded to the electronic board that allows the configuration / programming of the working points of the chip as well as the connection to power supplies and measuring instrumentation such as the oscilloscope. The chips that are selected to be bonded to their respective electronic boards must have undergone a test period in the probe station and ensure that they are working correctly. Once on board, tests are performed again before proceeding with taking measurements to verify that the bonding was done correctly. It is preferable to scan the parameters in the effective range of the detector to determine the best performance points and avoid subjecting the chip to too much stress and causing damage.

In the case of this work, we sought to characterize at least one of the boards with chips from the same batch. The four boards that were prepared for study and characterization

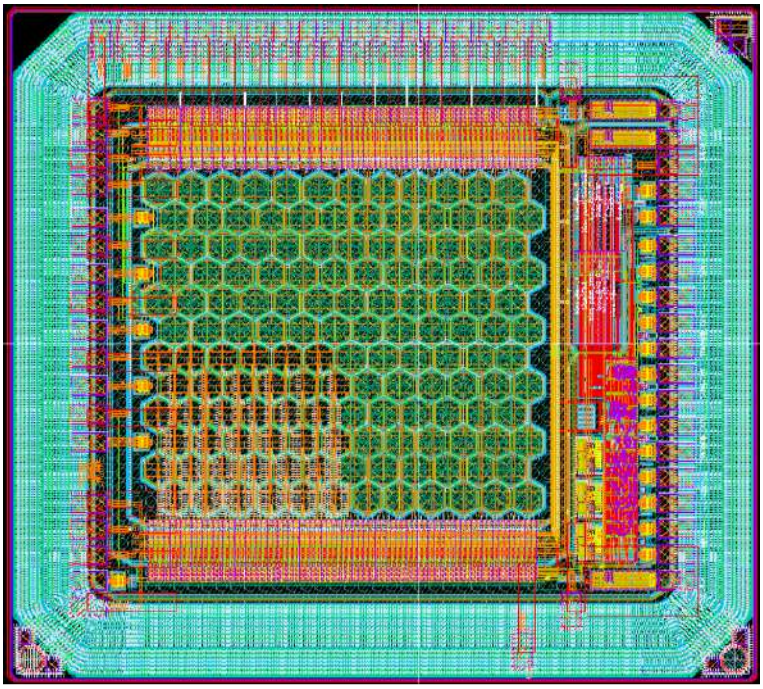

Figure 2.7: Design of the prototype chip for the ATTRACT project [25].

were labeled **Board 111**, **Board 112**, **Board 113** and **Board 114**. The board labeled **Board 114** was the one that was investigated in this thesis work.

It should be noted that these chips are characterized by having a thickness of $60\mu m$ in the case of Boards 111, 113 and 114, and $100\mu m$ in the case of Board 112. and a substrate resistivity of $50\ \Omega \cdot cm$. In all cases, the chips were manufactured without a gain layer.

On the other hand, an ATTRACT prototype with an experimental avalanche gain layer was also characterized. The chip that was chosen to be wire-bonded to the electronic board was called **Board 6439**. This one sample belongs to a series of chips designed with different doping characteristics, thickness of the boron-doped epitaxial (epi) layer, and masking of the gain layer.

The epi layer is a crystalline structure that is grown into a seed substrate in order to achieve a preferential orientation of the crystal lattice.

CHAPTER 3

Experimental methodology

The main objective of this work is to characterize the time response of the amplifier of the ATTRACT prototype using a pulsed laser. For this, we considered the variables of amplitude of the signal, production of charge inside the sensor, noise RMS, and signal-to-noise ratio.

Also, we seek to approximate the conditions under which the chip is subjected, to those of a detector in presence of an MIP radiation source, and then obtain the time resolution under these conditions.

3.1 Experimental setup and laser calibration

For the experimental setup and the data taking, the following devices were used:

- Monolithic silicon chip wire-bonded to its electronic board.
- Infrared picosecond pulsed diode laser, by NKT Photonics (PILAS DX) with < 3 ps RMS time jitter and wavelength $\lambda = 1057$ nm [26].
- 3-axes micrometric motor to adjust laser beam.
- LeCroy WaveRunner 610Zi, 1 GHz bandwidth and 20 GS/s sampling rate Oscilloscope [27].

- LeCroy WaveMaster 820Zi-A 610, 20 GHz bandwidth and 4× 40 GS/s sampling rate Oscilloscope [28].
- Power supplies for high and low voltages on detector configuration [29, 30].

In Figure 3.1, the measuring instruments listed above are shown.

(a) Oscilloscope

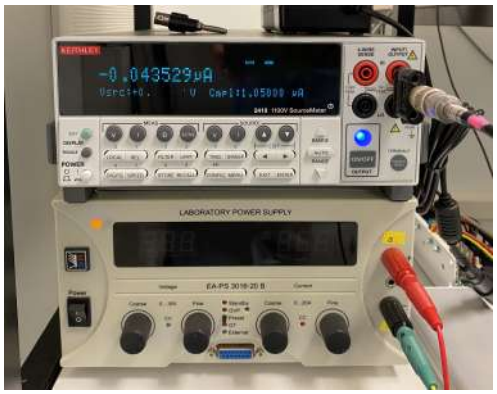

(b) Power supplies

(c) Laser

Figure 3.1: Measuring instruments used in the experimental setup and measurements.

First of all, the equipment setup was prepared, the detector was mounted on its frame structure, and a fine calibration of the laser equipment was carried out. The laser allows the selection of the relative intensity of the light that goes from 0 % (higher intensity) to 100 % (lower intensity) in steps of 0.01 %. In the next chapters and for the sake of simplicity, we will refer to intensity as 1−relative intensity, so the highest intensity reported corresponds to a 100%, and the lowest to a 0%.

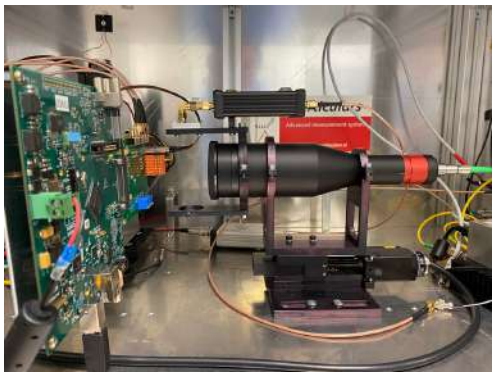

(a) Laser setup with electronic board, front view.

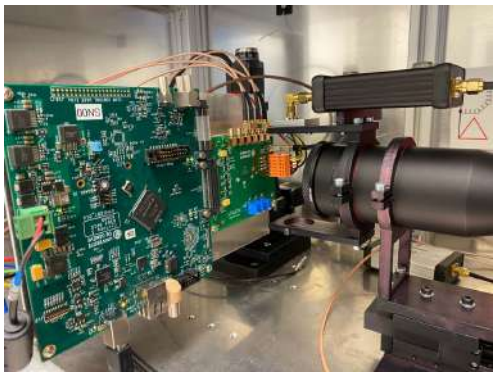

(b) Laser setup with electronic board, side view.

Figure 3.2: Laser and board experimental setup.

The setup of the laser with respect to the board is shown in Figure 3.2. With the help of three micrometric motors, the laser was calibrated with great precision along the x, y and z directions, as shown in Figure 3.3.

Care was taken that the frame that supports the detector was completely perpendicular to the laser beam to maximize its intensity and keep the light spot as small and precise as possible. This with the aim of firing the signal in only one of the pixels at a time.

The chip in question has four hexagonal pixels that correspond to four analog channels, which are the subject of interest of these measurements.

As mentioned above, for all measurements carried out with the laser, the beam was focused on only one of the pixels, typically the one that has been connected to analog channel 0. With the help of the 3-dimensional micrometric motors, and the shutter on the front of the optic's element of the laser, it was sought to maximize the amplitude of the pulse generated by analog channel 0 and to minimize the amplitude of the remaining 3 channels, thus avoiding, as far as possible, cross-talk effects.

Once the laser and the board are in the desired position and it is confirmed that the pulse amplitude is the maximum that can be obtained, the working point is configured, and the high and low voltages in the power supplies are set.

The intensity of the laser is determined and the obtained pulses (waveforms) are observed in the oscilloscope for the four analog channels. An example of laser waveforms for intensities of 100% and 50% are shown in Figure 3.4. Remember that channel 0 must have maximized

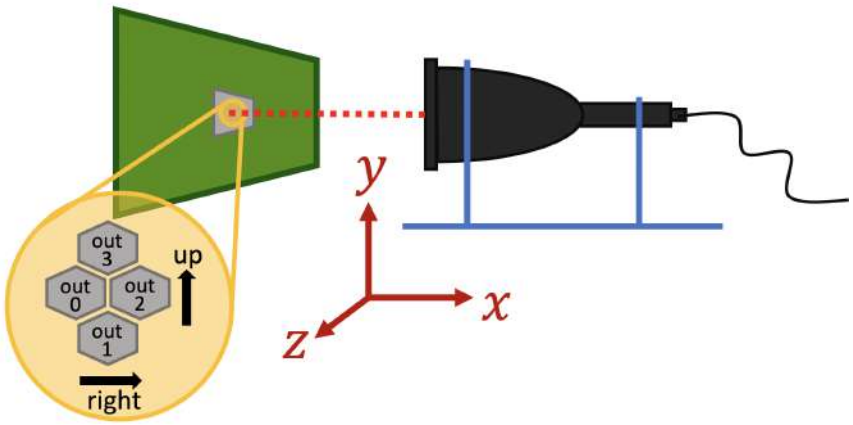

Figure 3.3: Diagram of the relative position of the chip's analogue pixels with respect to the laser and micro-metric adjusting motors in x, y and z axes.

amplitude and channels 1, 2 and 3 must have minimized amplitudes. Finally, the events are saved for a subsequent statistical analysis of the data.

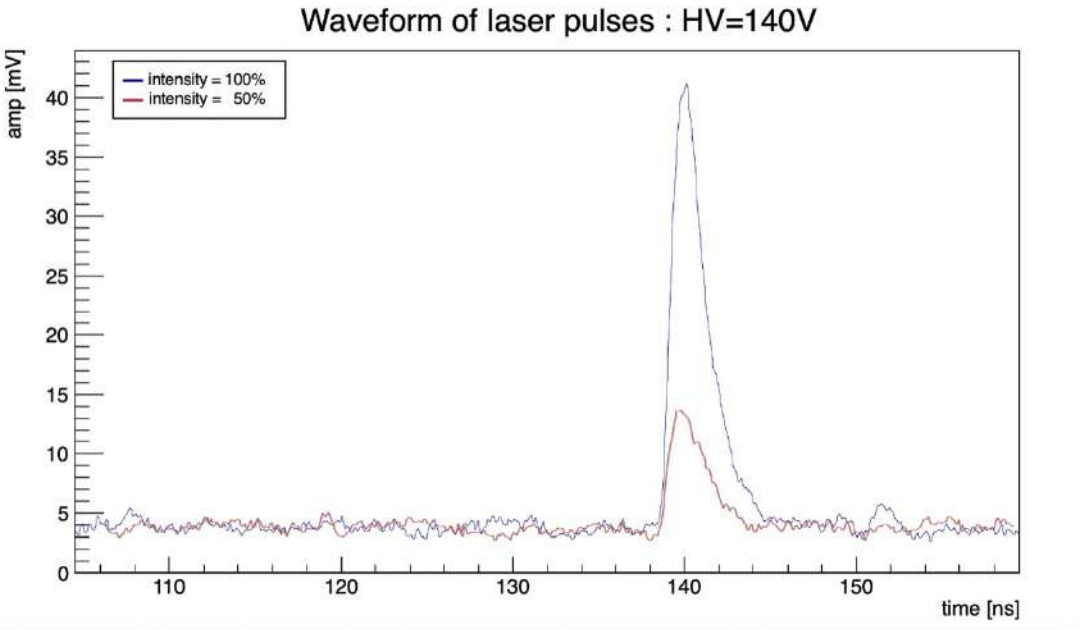

Figure 3.4: Laser event waveforms observed at an intensity of 100% (blue) vs. an intensity of 50% (red).

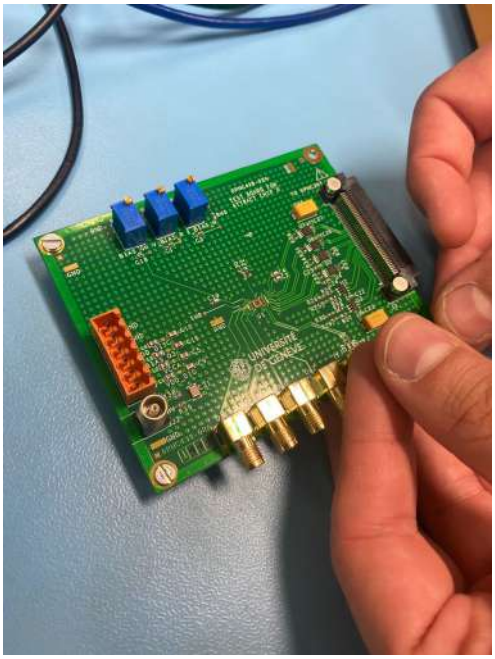

Figure 3.5: Photograph of the ATTRACT chip wire-bonded to Board 111.

3.2 Working point selection and configuration

The chip working point must be selected and configured before the start of measurement taking. The values contemplated to determine the working point and characterize the chip along the different allowed / functional values are shown in Table 3.1:

Values for working point election				
name	description	range	units	equivalence
−HV	High voltage applied to the surface of the chip	80-180	[V]	-
Vcc	Low voltage	1.7-2.0	[V]	-
bias_preamp	pre-amplifier bias current	0-255	[DAC]	0-255 μA
bias_feedback	feedback bias current	0-255	[DAC]	0-16 μA
bias_driver	driver bias current	0-255	[DAC]	0-255 μA

Table 3.1: Parameters to determine working point.

In general, the values of the selected working point are modifiable in a range that is shown in the third column of Table 3.1. Therefore, as an initial stage of the project, a scan of the sensor's behavior was carried out along the ranges of each of the given values, thus being able to characterize the detector in a general and broad way at the relevant

working points.
In the next pages, it will be common to refer to the working point (WP) as a set of three numbers divided by dashes. This notation corresponds to the values of preamp current - feedback current - driver current, in that order. For example, if allusion is made to WP = 150-100-100, for this we must understand that the working point into consideration has a preamp current of 150 μA, a feedback current of 100 DAC and a driver current of 100 DAC.

3.3 Data interpretation and statistical analysis with ROOT C++

Once the waveform data has been acquired with the oscilloscope, it must be converted to a format that facilitates its manipulation and statistical analysis. The conversion of the data from a binary format (Word / Byte) to a *.root* format for easy manipulation was done by means of a C ++ script, which facilitated the work of statistical analysis.
With help of such script, the information from each of the waveforms stored in the oscilloscope is extracted and divided in an orderly manner so that it can be accessed and viewed quickly through ROOT [31]. ROOT is a C++ framework designed at CERN for data analysis and processing in the context of High Energy Physics.
Once the data has been converted, the program generates a list of standard variables and stores them in the file *.root*, which will be used in the future to analyze and characterize the behavior of the detector.

In Table 3.1 we can find the definition of some of the variables that characterize a waveform or a set of waveforms produced by the particles that enter the detector. To select the waveforms that will be saved as valid events, a threshold is configured, which is the minimum value that the pulse amplitude must reach. This threshold must be considerably higher than the background noise, but not too high so that the lower energy events, which generate smaller pulses, are not cut off, as this would bias the statistics and the results obtained. In general, it is sufficient to take a threshold equal to $5\sigma_V$, *i.e.*, five

Relevant variables for statistical analysis		
Name of variable	Name in analysis script	Description
Amplitude	amp	Pulse amplitude
Toa	toa	Signal Time of Arrival at custom fixed threshold
Tot	tot	Signal Time over Threshold at custom fixed
Time@20% (t20)	time_20const	Time at 20% of the pulse amplitude
Time@80% (t80)	time_80const	Time at 80% of the pulse amplitude
Risetime (20-80)	t80 - t20	Difference of time at 80% of amplitude and time at 20% of amplitude.
Noise RMS (σ_V)	rms_bck	RMS voltage of background noise
ENC	rms_bck*6250/amp	Equivalent noise charge: $\simeq \sigma_V \cdot Q_{in}$/amp
Slope (20-80)	amp*0.6/rise time	Slope of the increasig pulse signal from 20% to 80% of the amplitude
Toa jitter (σ_t)	sigma_t	Standard deviation of the approximated-to-gaussian distribution of the time of arrival

Table 3.2: Some of the standard variables that characterize the waveforms obtained with the oscilloscope. These variables can be statistically analyzed after acquiring thousands of events and converting them to a *.root* format.

times greater than the RMS voltage of the signal noise. Then, each variable is analyzed statistically through ROOT in order to obtain the average values of a set waveforms. Figure 3.6 shows the histogram obtained from measurements of the amplitude of the pulses created by 2200 acquired laser events. These measurements were taken with Board 114 on the main analogue channel, Channel 0, WP=100-50-200, Vcc=1.7V, HV= -140V and the highest laser intensity (100%). Under these particular conditions, we can see that most of the laser events that were observed in the oscilloscope are within a range of 32-38 mV, and their distribution can be approximated by a Gaussian function, which initially provides useful information about the value of the amplitude of laser events and its distribution. The mean value of the Gaussian fit function is 35.02 mV with a statistical error of 4.04×10^{-2} mV. Note that the value of the error is not the σ of the distribution, but rather the statistical error of correctly estimating this parameter associated to the gaussian fit. Therefore, this is the value and respective error that will be reported for this specific point. In order to characterize this detector, special attention was paid to time variables such as

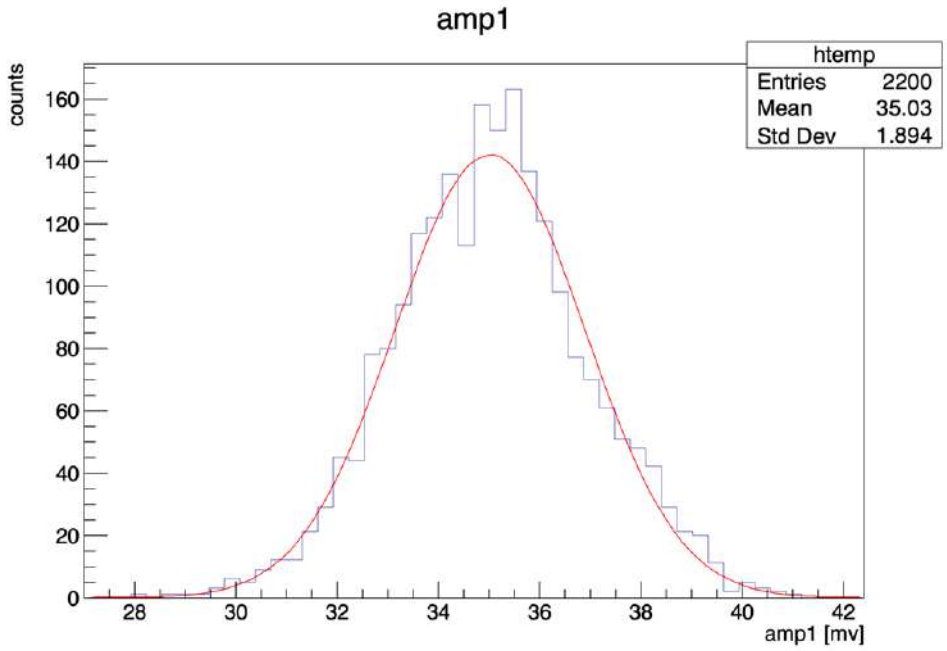

Figure 3.6: Example of histogram in ROOT showing the distribution of the amplitude of laser events recorded with the oscilloscope, to which a Gaussian fit was made.

the *time of arrival* (*toa*) and *time over threshold* (*tot*), since these are useful to characterize its time response.

3.4 Calculation of the time resolution by *toa* jitter and time-walk correction method

Time variables such as *toa* and *tot* provide relevant information regarding the time resolution of a particle detector. In the case of lasers, when using pulsed light with ultra-fast timing, each event will reach the detector with a pulse width of $20 - 110$ ps and a time jitter of < 3 ps RMS. As soon as radiation hits the detector, the charge generation and collection process initiates. Once the signal passes the threshold limit, the time of this precise moment is assigned to the *toa*. Therefore, we will associate the time resolution with the *toa* jitter that exists in a set of acquired laser events.

The *time walk* is a phenomenon that occurs because, due to the upward slope that a

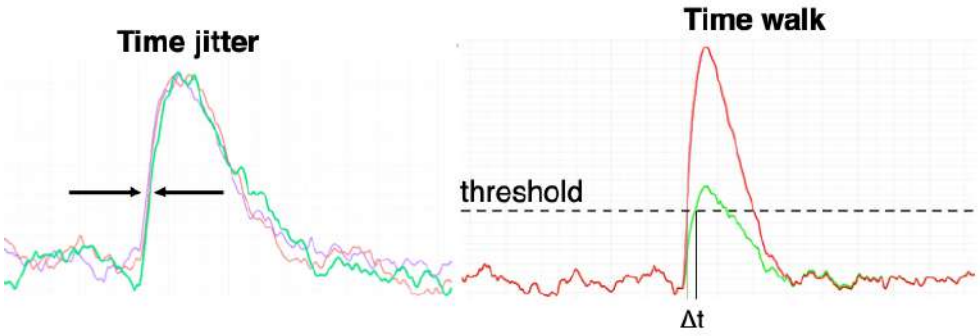

Figure 3.7: To the left: graphic exemplification of the time jitter given a certain threshold. To the right: time walk phenomenon that happens when pulses of different amplitudes have the same threshold [25].

pulse has before reaching its maximum, a fixed threshold is reached at slightly different times for pulses of different amplitudes. Such effect is illustrated in Figure 3.7.

Taking into account the time walk when acquiring a set of waveforms varying in amplitude, it follows that, in addition to measuring the *toa*, it is necessary to correct the effect caused by defining a fixed threshold.

The first thing to consider is the *toa* vs. *amp* relationship that can be viewed with the use of ROOT and the converted waveform data. If the points of *toa* vs. *amp* of each collected event are plotted, we will obtain a two dimensional histogram like the one shown in Figure 3.8(a).

Once this is done, it is possible to generate a profile plot, which is the graph of the average of *toa* for each bin of the amplitude, plotted with error bars that represent the standard deviation of the data from the central value. This type of graph is very useful to show behavior of the correlation between two variables.

Now, as can be seen in Figure 3.8(b), once the profile plot has been obtained, a function is fitted to the data to subtract the contribution of the time walk. In this case where a linear relationship is observed, such a function is fitted to the data, and its slope and y-intercept are determined.

Fitting a linear function to the relation *toa* vs. *amp*, the slope m and the ordinate to the origin b are obtained, then the distribution of the *toa*, after correcting the effects of the time walk, is given by the following expression:

$$toa_{corrected} = toa - (m \cdot amp + b),$$

which is exactly what is exemplified in Figure 3.8(c).

Finally, this distribution can, in general for the events acquired with the laser source, be fitted with a Gaussian function, from which its standard deviation σ will be considered by us as the time jitter σ_t which is what we consider to be the time resolution of the detector. Observe that this new variable cannot be obtained from a single waveform, but it is rather a statistical property of a data set.

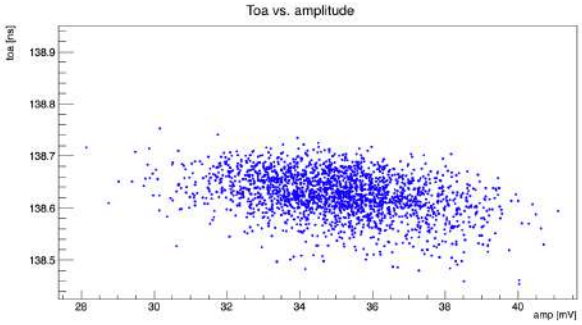

(a) Scatter plot of *toa* vs. *amp*.

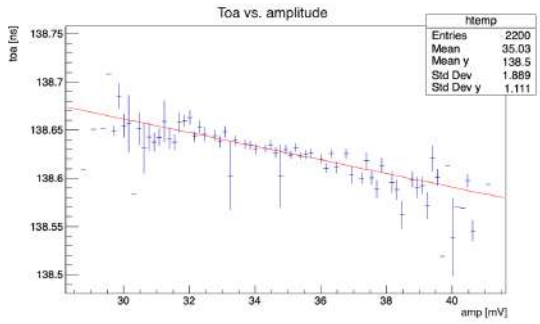

(b) Linear fit of profile plot *toa* vs. *amp*.

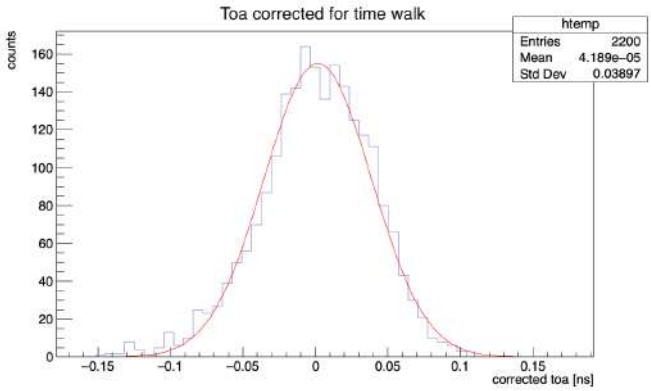

(c) *Toa* vs. *amp* distribution with linear correction of time walk.

Figure 3.8: Laser first measurements time resolution with *toa* corrected for time walk.

3.5 Calibration with ^{109}Cd radioactive source and first measurements

In order to calibrate the amount of charge generated inside the detector, a ^{109}Cd X-ray source was used. The photons emitted by the X-ray source are absorbed in the material of the detector via the photoelectric effect, thus generating a constant charge in the detector. Cadmium is an element that can be found in varieties of unstable radioactive isotopes that go through a gamma decay process, emitting photons with a well-known energy.

Due to the fact that the amount of energy deposited inside the detector is constant, we can make an approximation of the relationship between the amplitude of the signal observed in the oscilloscope with respect to the amount of charge (number of electrons) generated within the detector.

To illustrate the above, we can take a look at the energy spectrum of the particles emitted by ^{109}Cd. We know that the characteristic peak of higher energy in the cadmium spectrum

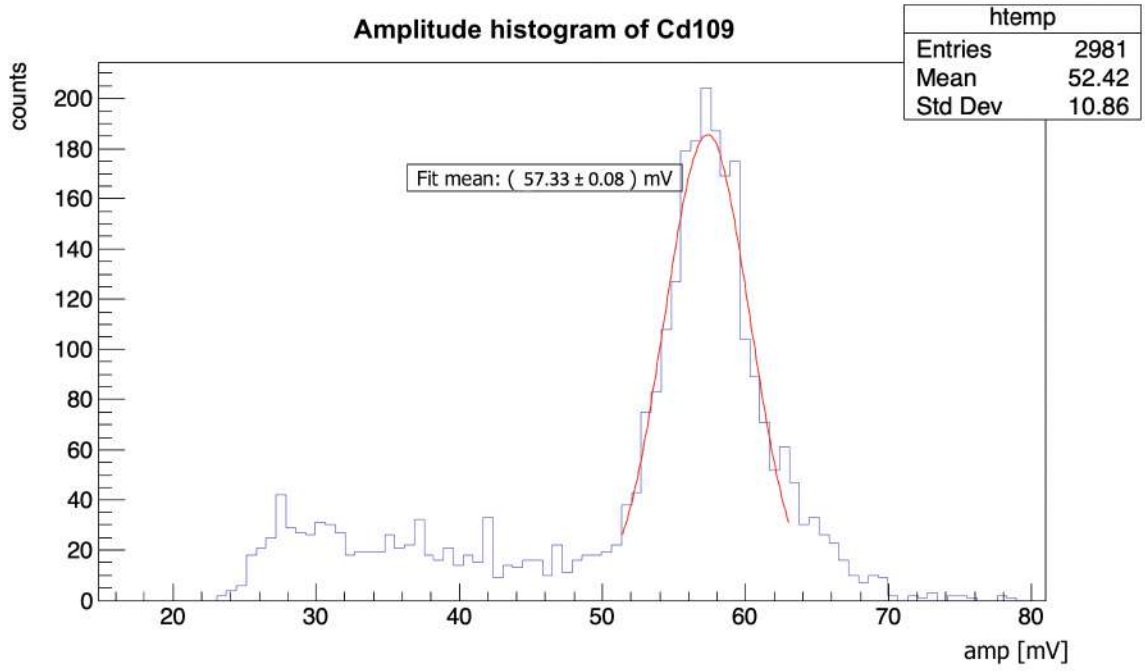

Figure 3.9: Example of the amplitude spectrum of a source of ^{109}Cd.

is equivalent to a charge generated within the detector of $\sim 1fC$, i.e. 6250 e^-.

As an example, we have the calibration performed for working point WP = 150-100-50 on Board 114 and HV= -120V. As seen in Fig. 3.9, the approximate amplitude of the maximum of the ^{109}Cd spectrum is 57.33 mV. It is then possible to find a relation between the intensity of the laser events, with their amplitude, and thus, to its energy and charge deposition. After the acquisition of the laser data, the ROOT histogram of the amplitude is taken and a Gaussian distribution is fitted. Considering again that the charge generated by the X-ray source of ^{109}Cd is constant, and that the amplitude of the signal is proportional to the energy, the following relation holds:

$$Q_{in} = 6250e^{-} \cdot \frac{amp}{57.33}, \tag{3.1}$$

assuming linearity is preserved.

3.6 Measurements with ^{90}Sr as a source of MIPs

Since this detector can be used as a detector for minimum ionizing particles (MIPs), it is important to consider the time resolution in front of a radiation source whose energy (amplitude) spectrum, is distributed as such. That is the case of the β^{-} particles emitted during the radioactive decay of ^{90}Sr, whose spectrum has a Landau distribution, so the behavior of the detector in the presence of particles of this type is particularly interesting. It is possible to deepen on the process of measurement and calculation of the times of flight (TOF) of the β^{-} particles emitted by the ^{90}Sr between the well-known reference LGAD (see Section 2.3) and our detector. The results for the TOF obtained on Board 114 for different working points can be reviewed in [32], and are showed for comparison in Section 4.2.

Because the behavior of a MIP inside the detector is not necessarily equal to the response of the detector to an incoming infrared photon, as is the case with particles emitted by the laser, a procedure was performed to mimic / reproduce the response of the detector in the presence of β^{-} radiation selecting events generated by the laser source.

The idea is to take a complete run of measurements acquired using the ^{90}Sr radioactive source and use it as a template. From the data obtained with the ^{90}Sr, we focus on the

amplitude distribution of the acquired events. This distribution can be visualized with a ROOT histogram like the one shown on Figure 3.10 b). Next, a code was created to take events generated with the laser when scanning the intensities and use them to reproduce the amplitude distribution of ^{90}Sr. Once the laser events have been redistributed to reproduce those of ^{90}Sr, they are processed to obtain the *toa* jitter, i.e. time resolution, of the detector.

3.6.1 Method of reproduction of ^{90}Sr spectrum by selection of laser events

In order to obtain time resolution results that are comparable to those produced by a source of MIPs, a selection and cut of the laser events was performed in order to reconstruct the spectrum of ^{90}Sr. This procedure was implemented in Board 114 for 2 working points.

First, the point WP = 150-100-50 was considered, with Vcc = 1.8V. Measurements of 1000 laser events per run were taken scanning the laser intensities from 100% to 25%, in variable intervals, as to increase the density of events near the maximum of the ^{90}Sr spectrum. This was done as follows:

Intensity scan from 25% to 100%

- 25% - 49% (1% steps i.e. 25 runs)
- 50% - 68% (2% steps i.e. 10 runs)
- 70% - 100% (3% steps i.e. 11 runs)
- TOTAL: 46 runs, 1000 events each.

Then all the acquired events were merged into a single file. An example can be seen in Figure 3.12, where the working point was WP=150-100-50, Vcc=1.8V and HV= -140V.

Even though the histogram in Figure 3.12 has an uneven distribution, the final result only depends on the events remaining after the selection and cut that is applied on them.

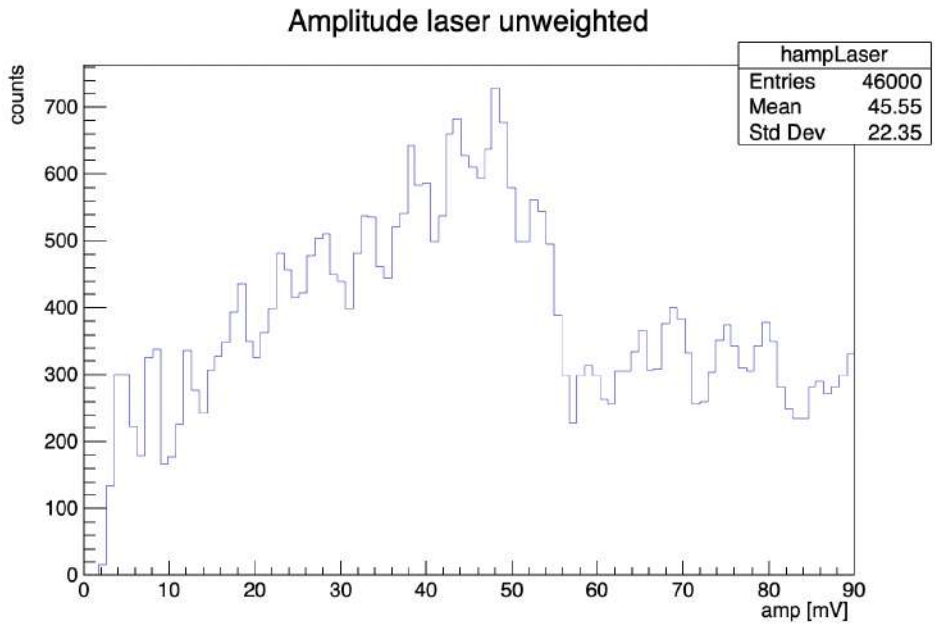

Figure 3.10: Amplitude histogram of merged laser events (46000).

The objective is to imitate the shape of the desired spectrum proportionally to the number of final events, and it was done through a C++ script. First, the histograms of the laser and the ^{90}Sr are taken on the same horizontal scale and with the same binning. The bin in which the maximum events in the ^{90}Sr spectrum are found is identified, and all laser events corresponding to that same bin are kept. This value determines the constant of proportionality between one spectrum and another. By rebinning the laser events histogram as in Figure 3.14, it can be verified that both spectra coincide.

Finally, the time resolution for this set of events was obtained with the same script that was used for the ^{90}Sr TOF analysis [32]. The results obtained are presented in Section 4.2.

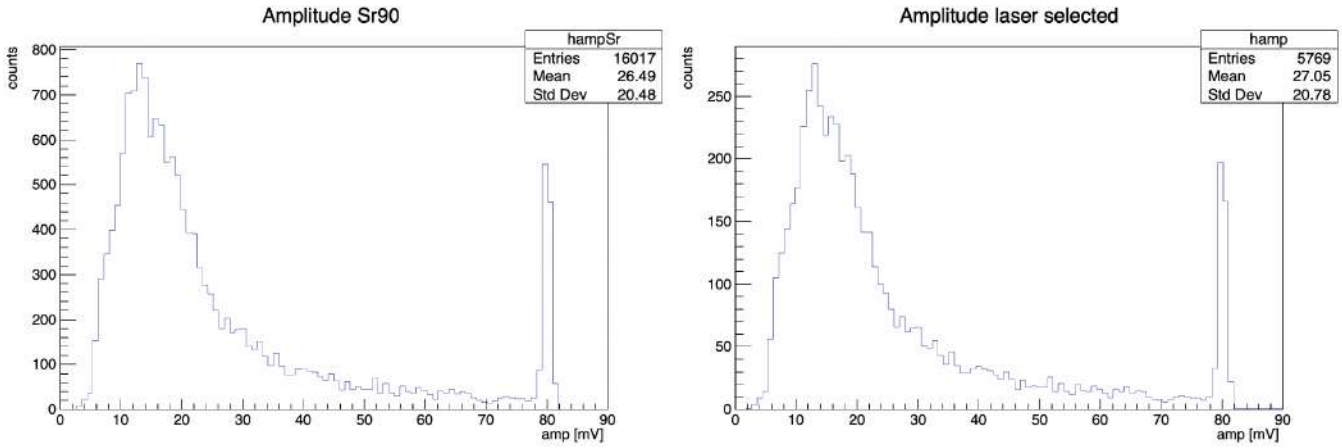

Figure 3.11: To the left, amplitude spectrum of ^{90}Sr. To the right, amplitude spectrum of laser selected events. Note that vertical scale is not the same in both histograms.

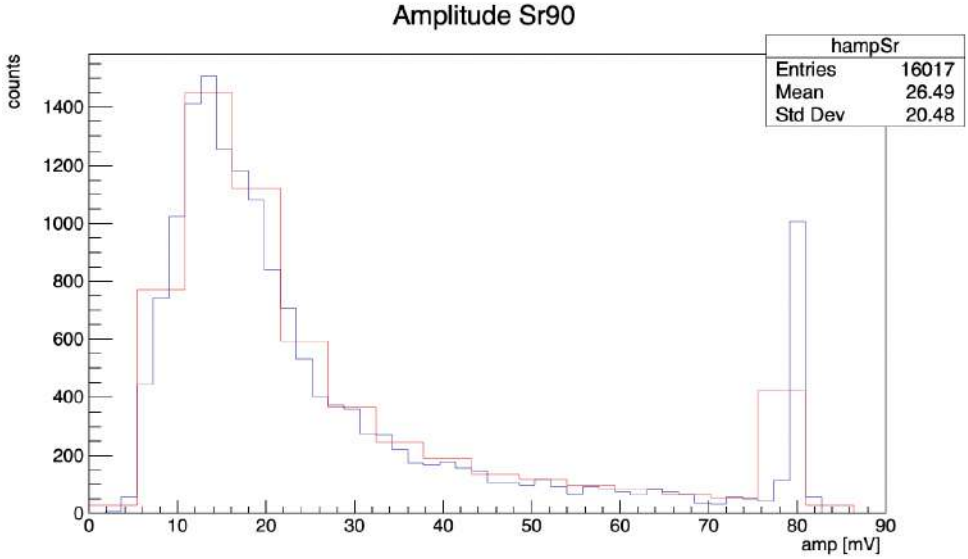

Figure 3.12: Superposition of both histograms shown in Figure 3.11. Laser histogram had to be rebinned in order to approximately match the number of events of the ^{90}Sr template in each bin.

CHAPTER 4

Results and discussion

This chapter is dedicated to summarize the results obtained in the series of measurements that were discussed in the previous chapter. Time resolutions of the Board 114 and Board 6439 were obtained at different working points in different configurations of high voltage HV and low voltage Vcc, as well as some other parameters of interest that were useful to characterize the waveforms of the ATTRACT prototype.

4.1 Characterization and timing resolution with laser source

First of all, a general characterization of the detector was made to determine which working points had the best response. An analysis was also carried out where, in addition to observing the time resolution obtained with the laser, other interesting variables were explored to characterize the signals. Such is the case of the *tot*, the background noise σ_V, ENC, and the amplitude vs. intensity and/or amplitude vs. charge. These variables are interesting because they represent factors that will also have a contribution to the final time resolution of the detector.

4.1.1 Board114

First measurements

The results reported below correspond to the first measurements made with the laser on Board 114. Measurements were taken for HV = −120V and HV = −160V at the working point WP = 150-50-200 and Vcc = 1.7V.

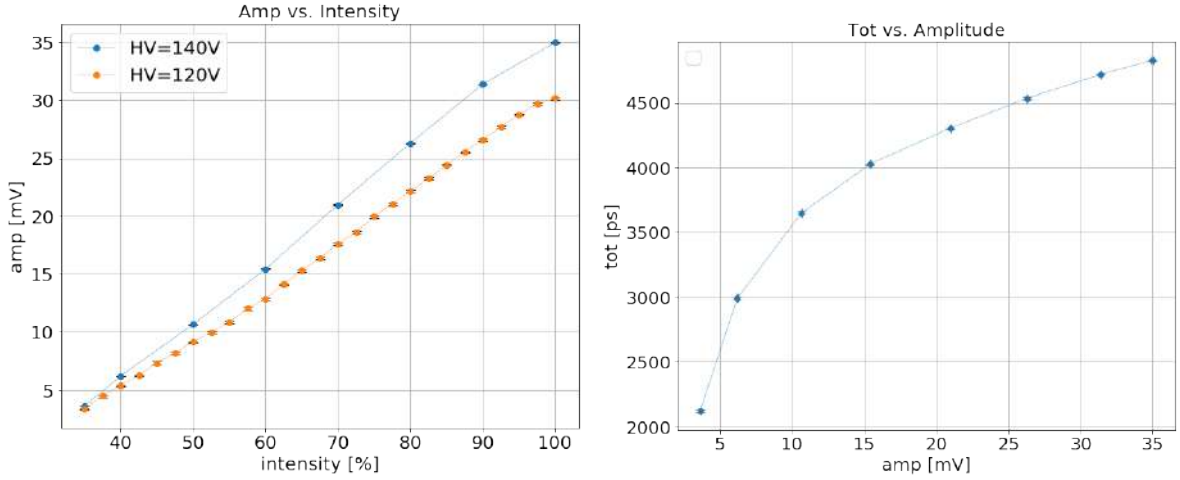

(a) Amp vs. intensity for HV = −140V (blue) y HV = −160V (orange).

(b) *Tot* vs. *amp* at HV= −140V.

Figure 4.1: Laser first measurements of *amp* and *tot* variables vs. laser intensity from 0% to 65%

The graphs of amplitude vs. intensity, *tot* vs. *amp* and time jitter with and without time walk correction are shown in Figures 4.1 and 4.2. These four plots illustrate the first attempt to characterize the amplifier and time response of the detector.

First of all, looking at the plot on Figure 4.1(a), we observe that the behaviour of the amplifier can be easily approximated with a linear fit as a function of the intensity of the source of radiation. The slope of such function depends on the HV applied to the sensor. Figure 4.1(b) shows the relation between amplitude and *tot*. The statistical error of the fitting parameters obtained for the gaussian fit on ROOT are plotted as the error bars. In Figure 4.2(a), on the other hand, the same points as in Figure 4.1(b) are plotted, with the difference that the error bars showed correspond to the standard deviation σ of the gaus-

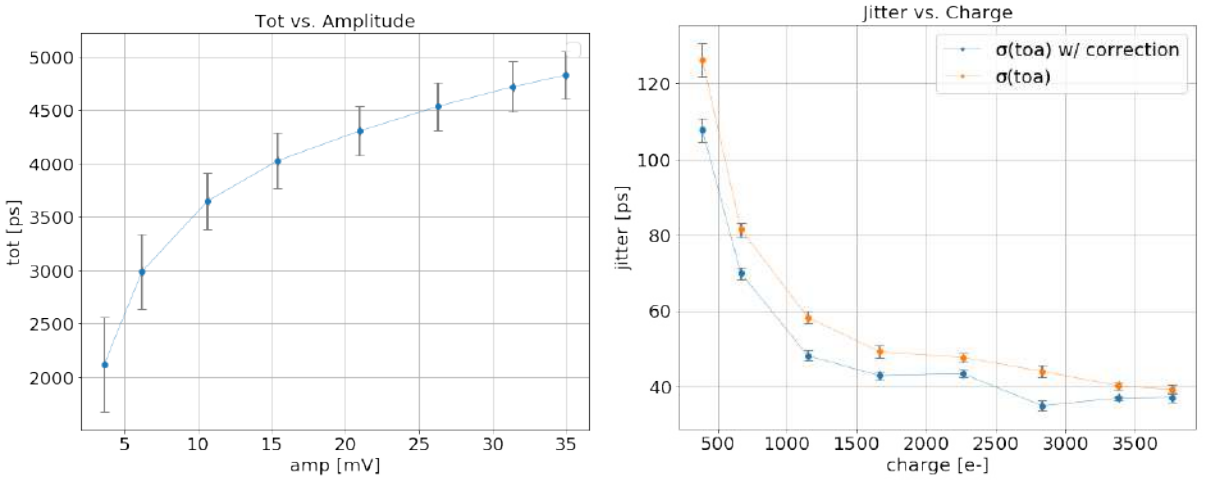

(a) *Tot* vs. *amp* with σ std dev as error bars.

(b) *Tot* jitter vs. charge with (blue) and without(orange) time walk correction.

Figure 4.2: First attempt to obtain a time resolution measurement at HV = 140V

sian fitting function determined by ROOT. This procedure was implemented to illustrate the behaviour of this particular variable as a reliable measure of the timing performance. In Figure 4.2(b), the values of *tot* jitter are shown for the previously discussed measurements, both with and without time walk correction as explained in Section 3.4. This plot shows the importance of doing a time walk correction to achieve better and more truthful results as we aim towards ultra-fast timing.

Second measurements

Below are the results of the second measurements made with the laser for the same working point as in the previous measurements, i.e., WP = 150-50-200. A scan on the intensities going from 100 % to 65 % was made for values of HV = −80V, −100V, −120V, −140V, −160V, and −180V. Figure 4.3 (a) shows the results obtained for amplitude vs. intensity, while in Figure 4.3 (b) the values of the *toa* jitter were obtained without the use of the capacitor in the connection of the oscilloscope in blue, while the orange points show the results once the capacitor of C = 100nF was implemented. This capacitor was adapted in the transmission line connecting the analogue out channels of the board together with the oscilloscope. Since the results of both time jitter, the noise-signal ratio and the signal susceptibility to oscillations improved considerably with the use of the capacitor, it was

decided to keep this modification in the future.

Figure 4.3(a) reinforces the result obtained in Figure 4.1(a) that the relation *amp* vs. intensity is linear and its slope depends on the HV for a same WP.

The increase of the HV from −80V to −180V results in a constant increase in the slope of the linear behavior of the amplitude, which means that the charge production is also constantly increasing without reaching a limit or saturation charge inside the detector. Therefore, we can say that, in this range of high voltage, the sensor is never fully depleted.

In Figure 4.3(b), *toa* jitter is plotted for HV from −80V to −180V in 20V steps. These results were taken with a 90% laser intensity in all the cases to see the behaviour of the *toa* jitter with respect to the HV. From this point on, the variable to take into account with regard to the time resolution, will be the *toa* to keep consistency throughout the rest of the work.

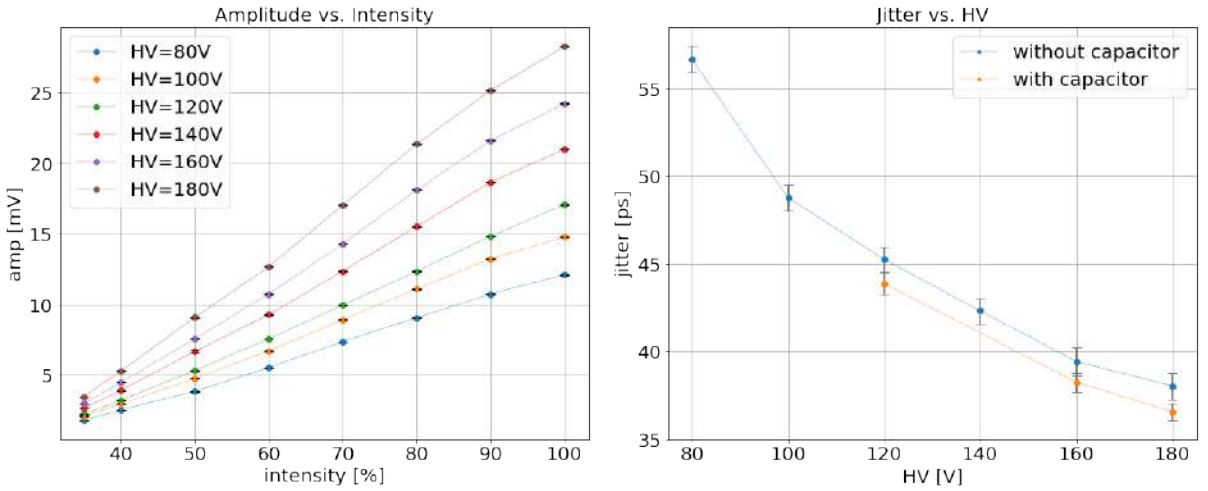

(a) Amp vs. intensity measurements for HV= −80V, −100V, −120V, −140V, −160V, and −180V.

(b) *Toa* jitter vs. HV at intensity of 90%. Measurements without capacitor are shown in blue, and with added capacitor are plotted in orange.

Figure 4.3: (a) Plots of the relationship of amplitude vs. intensity for different HVs are shown. (b) The first results of *toa* jitter as a measure of time resolution is presented. In both cases, WP=150-50-200.

The aim of presenting Table 4.1 is to have the numerical results of the measurements to consult, and help the reader to compare the values of different variables when the chip is under different conditions.

Board 114 Laser Time Resolution Summary Table: WP=100-50-200 bias_preamp = 100μA, bias_feedback = 50 DAC, bias_driver = 200 DAC, Vcc = 1.7V					
−HV [V]	Intensity [%]	With capacitor	Amplitude [mV]	charge [e-]	Time resolution Toa jitter [ps]
140	100	No	34.97 ± 0.05	3770.28 ± 5.52	37.09 ± 1.26
140	90	No	31.38 ± 0.03	3383.43 ± 3.43	36.94 ± 0.65
140	80	No	26.28 ± 0.04	2832.98 ± 3.82	34.92 ± 1.33
140	70	No	20.99 ± 0.03	2262.84 ± 3.40	43.41 ± 0.97
140	60	No	15.42 ± 0.05	1661.88 ± 5.37	42.89 ± 1.05
140	50	No	10.65 ± 0.02	1148.46 ± 2.31	48.12 ± 1.35
140	40	No	6.19 ± 0.02	667.73 ± 2.11	69.86 ± 1.61
140	35	No	3.61 ± 0.01	389.46 ± 1.51	107.71 ± 3.03
80	90	No	10.76 ± 0.02	1159.52 ± 2.96	56.67 ± 0.77
100	90	No	13.25 ± 0.02	1428.06 ± 2.63	48.77 ± 0.75
120	90	No	14.86 ± 0.04	1601.78 ± 4.05	45.25 ± 0.69
140	90	No	18.67 ± 0.03	2012.74 ± 3.14	42.32 ± 0.72
160	90	No	21.63 ± 0.03	2331.42 ± 3.53	39.43 ± 0.82
180	90	No	25.17 ± 0.05	2713.69 ± 5.01	38.04 ± 0.77
120	90	Yes	14.86 ± 0.04	1601.78 ± 4.05	43.87 ± 0.62
160	90	Yes	21.63 ± 0.03	2012.74 ± 3.53	38.26 ± 0.54
180	90	Yes	25.17 ± 0.05	2713.69 ± 5.01	36.56 ± 0.49

Table 4.1: Results on first attempts to measure time jitter.

Parameter scan

Once the working method was established, and having improved the behavior of the signals for a variety of working points with the use of the 100nF capacitor, a scan was performed on the preamp, feedback and driver currents at HV= −120V constant and Vcc= 1.7V. The explored values of the bias currents were the following:

- Preamp = 10, 50, 100, 200 [μA]
- Feedback = 10, 50, 100, 200 [DAC]
- Driver = 50, 100, 200 [DAC]

The results obtained were graphed and shown below.

From these plots we note that not every working point previously defined in the ranges of the bias currents are present. This is because, in spite of the use of the capacitor,

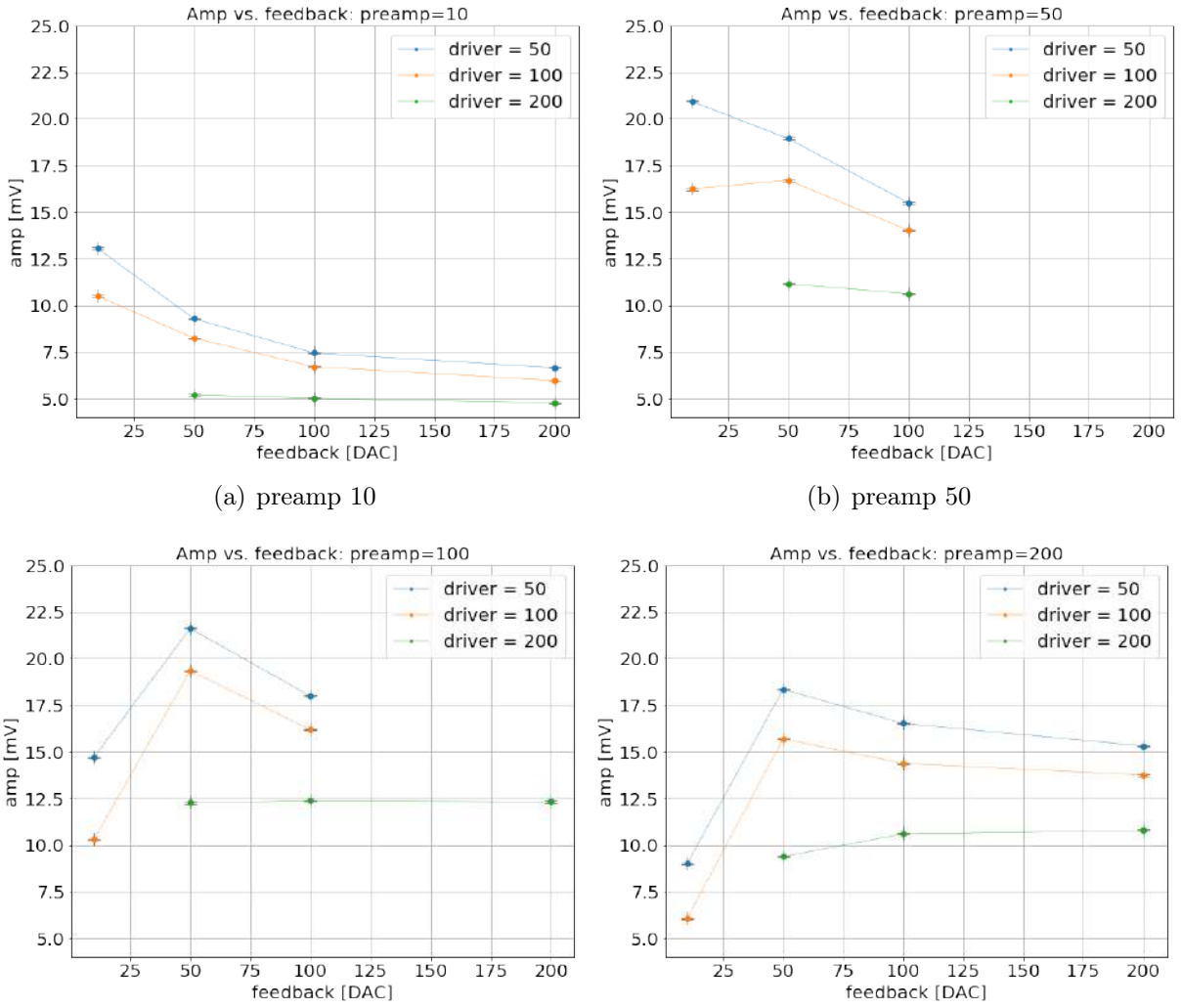

(a) preamp 10

(b) preamp 50

(c) preamp 100

(d) preamp 200

Figure 4.4: Working points broad scan on Board 114: *amp* vs. feedback with preamp values 10, 50, 100, 200.

some of the working points were inevitably unstable and/or presented important signal oscillation. Whenever this is the case, it is better not to take measurements because the results will be unreliable or misleading.

In the set of four plots shown in Figure 4.4, we are looking for the best relation preamp-feedback-driver bias currents. The objective is to achieve configurations that give high values of amplitude, but at the same time trying to minimize the power consumption of the working point, which means low values of preamp and feedback currents. Figure 4.4(c) shows the measurements of the mean signal amplitude *amp* vs. the feedback current for

different configurations of preamp and driver currents.

From these data points, the maximum amplitude measured was achieved applying the following bias currents: bias_preamp= 100μA, bias_feedback= 50 DAC and bias_driver= 50 DAC. This result, as already stated before, only gives us information of the pulse amplitude, but to have the whole picture, we must have a look to the ENC and noise values on Figures 4.5 and 4.6.

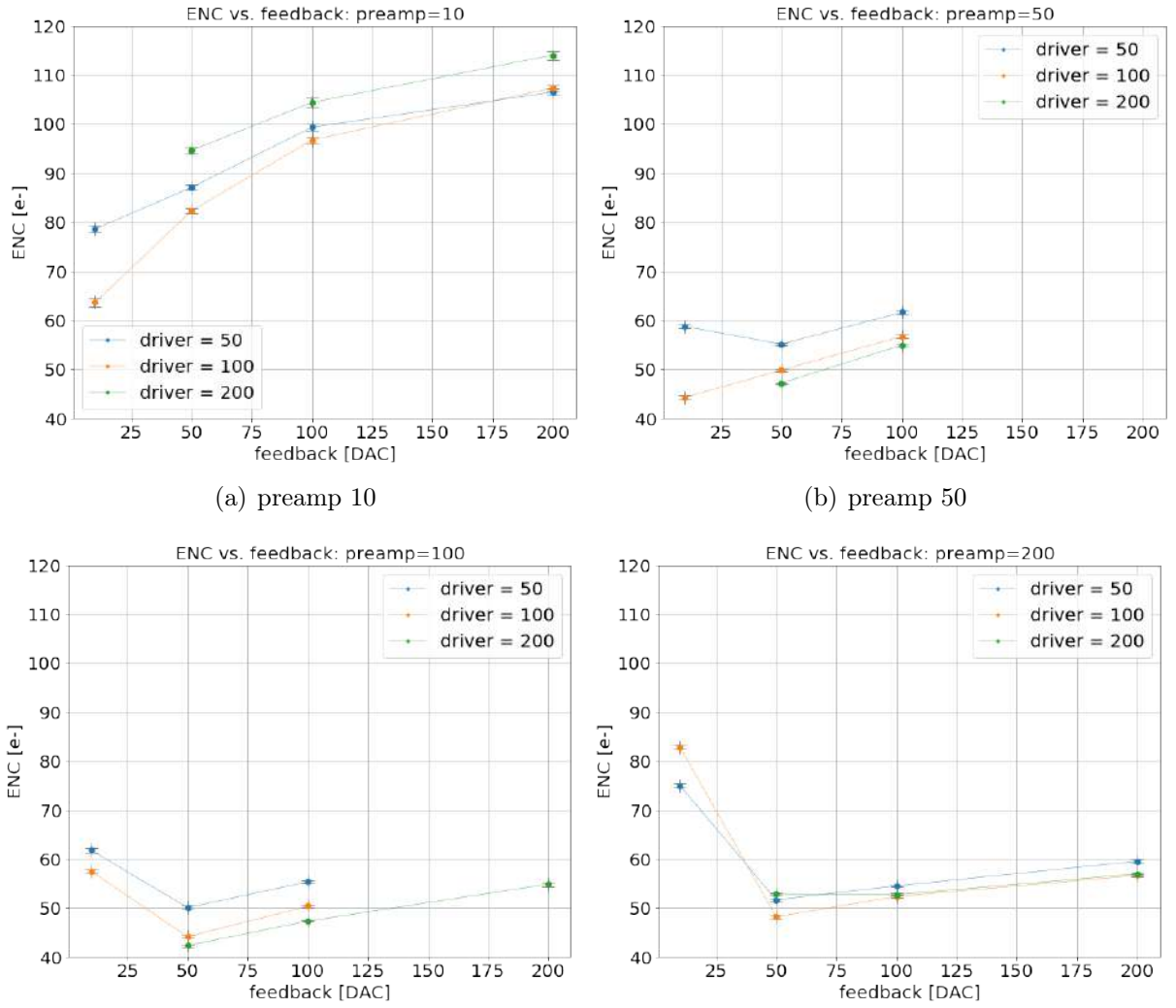

(a) preamp 10

(b) preamp 50

(c) preamp 100

(d) preamp 200

Figure 4.5: Working points broad scan on Board 114: ENC vs. feedback with preamp values 10, 50, 100, 200.

In Figure 4.5, we have the same working points plotted to show the relation of ENC

vs. feedback for four different values of bias_preamp. In general, these plots show that for lower values of preamp currents, lower values of feedback will reduce the ENC produced in the chip. Again, for high power consumption we find that the best value for feedback current is around 50μA, and we notice that higher values of driver current improve the ENC values. In Figure 4.5(c), it is shown that values of bias_driver = 100 DAC and 200 DAC lower the ENC considerably with respect to a bias_driver of 50 DAC. A preamp current of 200μA does not improve the behaviour of the chip neither in the amplitude or ENC values. However, for low power consumption working points of a preamp current of 10 μA, the relation of the ENC vs. the feedback is better with the lowest measured value of the feedback, at bias_feedback = 10 DAC. Finally, we want to see the behaviour of the signal noise with respect to the intrinsic noise of the oscilloscope. This value is taken always before setting the working point, and without any kind of signal being sent to the device. In this case, the value of the intrinsic noise of the oscilloscope is of $\sigma_V = 0.273mV$. Results of the noise measurements for the same WPs are shown in Figure 4.6.

It is desirable that the RMS noise is not too close to the intrinsic noise of the oscilloscope, because if that is the case, the noise contribution to time resolution cannot be well differentiated between signal noise and intrinsic noise. In Figure 4.6 we observe that in all cases, higher driver currents decrease the levels of noise, almost reaching the intrinsic minimum value when bias_driver = 200 DAC and bias_feedback = 50 DAC.

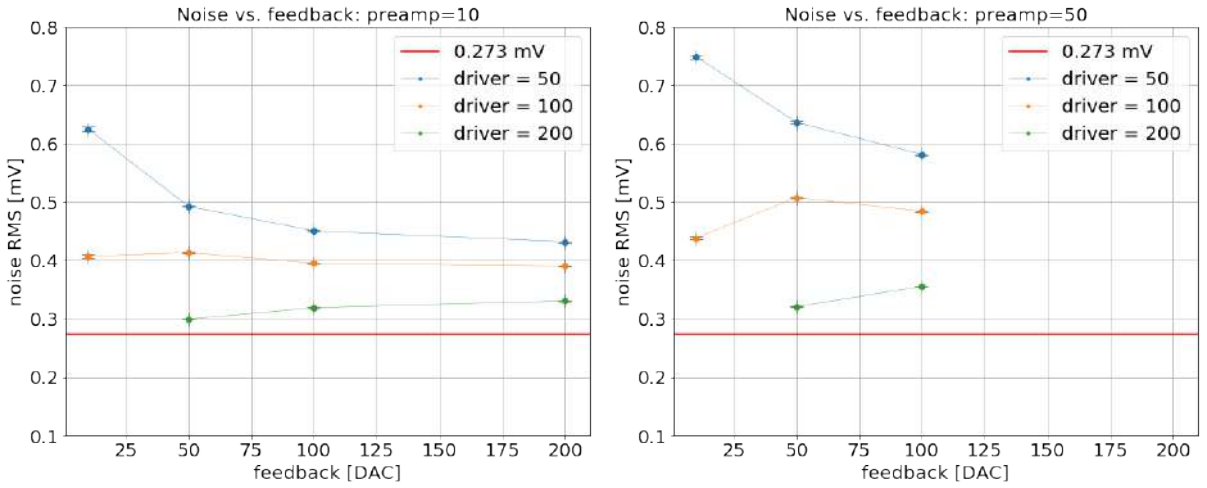

(a) preamp 10

(b) preamp 50

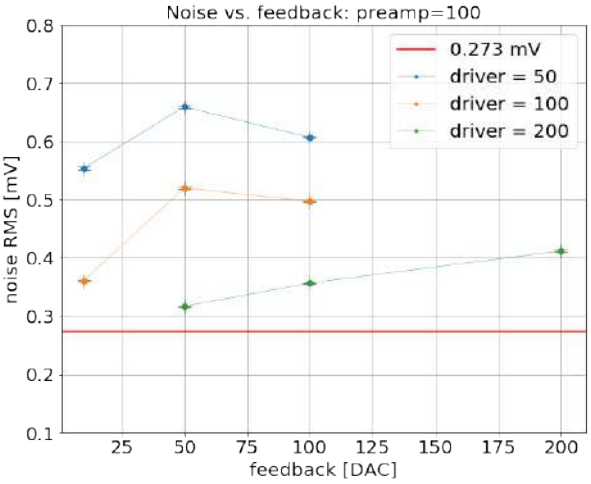

(c) preamp 100

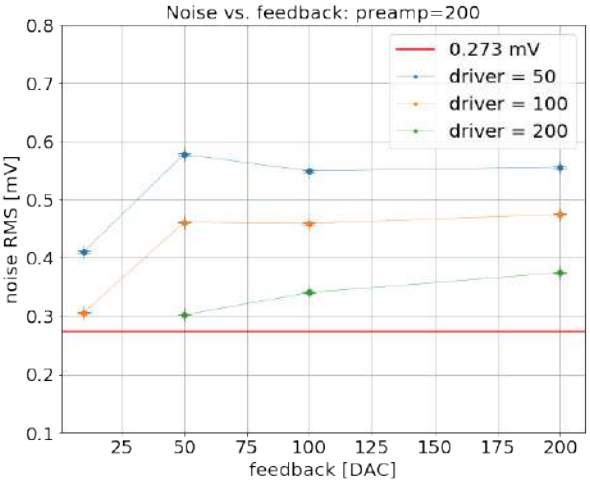

(d) preamp 200

Figure 4.6: Working points broad scan on Board 114: Noise vs. feedback with preamp values 10, 50, 100, 200.

WPs high power consumption

The results that follow correspond to measurements made for the working point WP = 150-100-100, Vcc = 1.7V and HV = −100V, −120V, −140V, −160V, and −180V. Based on the WP scan showed previously, this point was selected to deepen its amplifier and time response characterization. Figure 4.7 shows the plotted results for the amplitude measurements, as well as estimating the charge generated inside the detector for each intensity of the laser.

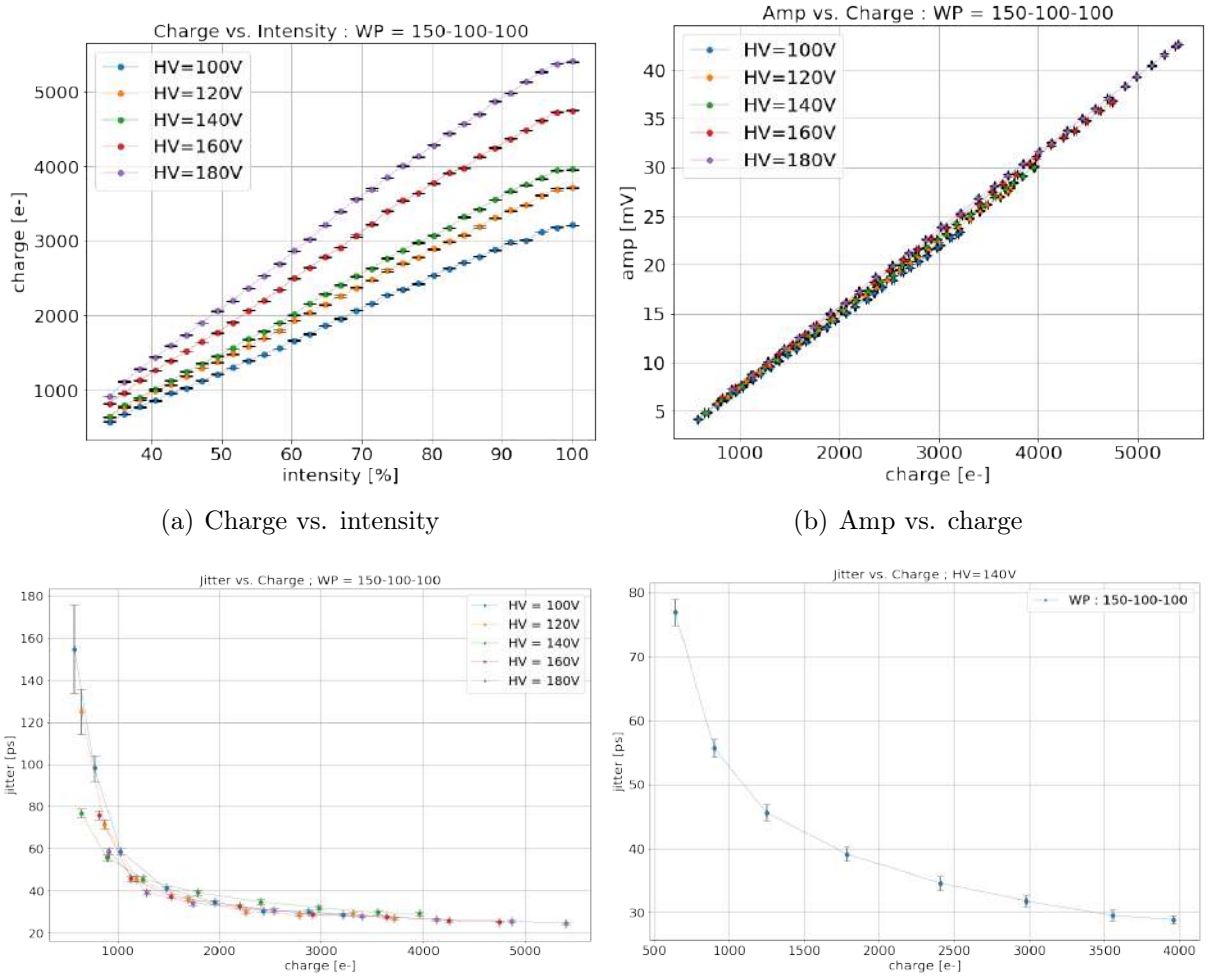

(a) Charge vs. intensity

(b) Amp vs. charge

(c) *Toa* jitter

(d) *Toa* jitter at HV = −160V

Figure 4.7: Measurements for WP 150-100-100 at different HVs.

Figure 4.7a) reinforce the fact that the charge production inside the sensor is linear with the laser intensity and it does not fully deplete at up to −180V. In Figure 4.7b) we can see that the production of charge is proportional to the amplitude and does not depend on the HV in this range. Higher HVs were not used because of the risk of breakdown of the sensor, which was observed in the probe station near 200V.

Figure 4.7c) and 4.7d) shows the *toa* jitter as a function of the charge produced for different HVs. Its clear that timing resolution improves with higher laser intensities and charge production, however, we can see in Figure 4.7c) that, for this configuration, the *toa* jitter reaches a hard limit around 20ps.

Table 4.2 shows that the best values of amplitude and *toa* jitter for this working point

Board 114 Laser Time Resolution Summary Table: High Power Consumption WP=150-100-100, C=100nF, Vcc=1.7V				
−HV [V]	Intensity [%]	Amplitude [mV]	charge [e-]	Time resolution Toa jitter [ps]
100	100	23.39 ± 0.05	3213.55 ± 5.94	28.51 ± 0.68
100	67	14.24 ± 0.04	1955.26 ± 5.22	34.49 ± 0.93
100	34	4.17 ± 0.04	574.53 ± 4.75	154.86 ± 21.14
120	100	27.89 ± 0.06	3717.56 ± 5.93	26.67 ± 0.66
120	67	16.90 ± 0.05	2260.56 ± 6.34	29.97 ± 0.79
120	34	4.82 ± 0.03	645.12 ± 3.77	125.11 ± 10.75
140	100	30.10 ± 0.05	3962.56 ± 5.80	28.86 ± 0.67
140	67	18.27 ± 0.04	2408.13 ± 5.53	34.59 ± 1.14
140	34	4.82 ± 0.04	640.96± 4.75	78.89 ± 2.06
160	100	36.82 ± 0.06	4746.53 ± 7.68	25.11 ± 0.59
160	67	22.66± 0.06	2915.24 ± 7.92	28.66 ± 0.67
160	34	6.35 ± 0.03	819.52 ± 3.47	75.79 ±2.28
180	100	42.61 ± 0.05	5405.29 ± 6.77	24.25 ± 0.54
180	67	26.80 ± 0.07	3398.38 ± 5.81	27.71 ± 0.68
180	34	7.26 ± 0.03	913.45 ± 4.34	58.58 ± 1.44

Table 4.2: Summary table for high power consumption working points.

were, as expected, with the highest HV and intensity, which gave a result of 24.25ps of time resolution, with a pulse average amplitude of 42.61mV and an estimated generation of charge of $5405.3e^{-}$. The worst performance were at the lowest HV applied and with the lowest laser intensity. Results show that under this conditions, the time resolution is of 154.86ps, the average pulse amplitude is 4.17mV, and a charge equivalent of $554e^{-}$.

The following results were again measurements taken for the working point
WP = 150-100-100 with values of HV = −100V, −120V, −140V, −160V, −180V sweeping at laser intensities from 100% to 66% in steps of 2.2%.
The working points WP = 150-50-50 and WP = 100-50-50 were also characterized, in both cases with values of HV = −100V, −120V, −140V, −160V, and Vcc = 1.7V.
Amplitude-intensity-charge, noise, and *toa* jitter analyzes were performed and the results are illustrated in Figure 4.8.

Figure 4.9 shows the comparison of the results obtained with respect to amplitude-charge-intensity, noise and *toa* jitter for the working points WP = 150-100-100,
WP = 150-50-50 and WP = 100-50- 50, in all cases with HV = −160V and Vcc = 1.7.

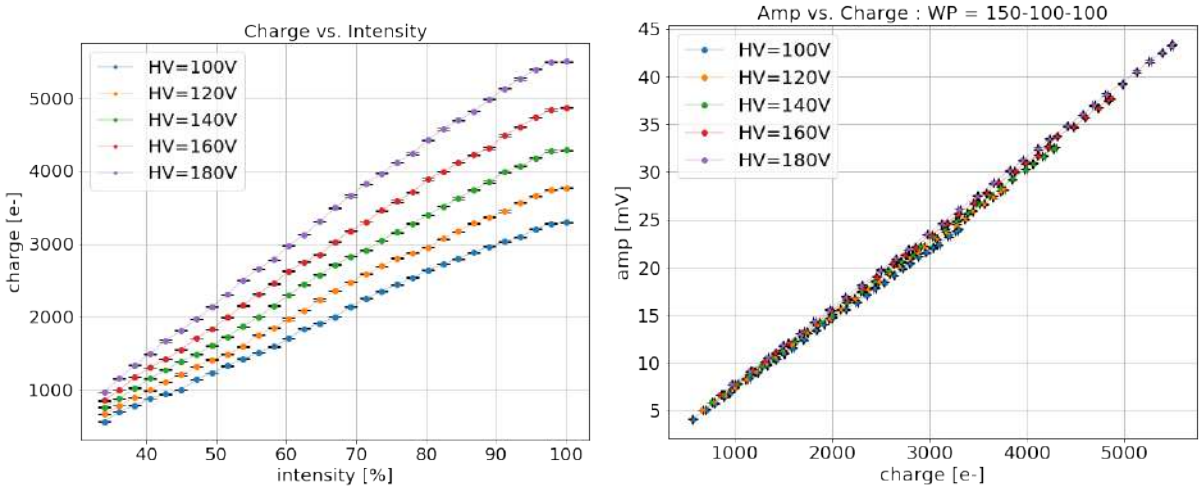

(a) Charge vs. intensity

(b) Charge vs. *amp*

Figure 4.8: Measurements of amplitude-charge-intensity fot WP=150-100-100 in HV = −100V, −120V, −140V, −160V, −180V.

Table 4.3 shows the results obtained for three working points in the high power consumption range. However, note that working points with higher preamp currents not necessarily translate in higher signal amplitudes and/or lower time jitters. This is why is important to check the waveforms of the events acquired and to make comprehensive measurements that give an idea of the behaviour of working points in a range of values.

From these 3 different working points, we observe that the one with best performance with respect to time resolution, is the WP = 150-100-100, even if this same point presents the lowest amplitude vs. charge relation. Also, the noise from the signal is below two times the intrinsic noise from the oscilloscope, which means that a big part of the ENC comes from the oscilloscope and not from the amplifier. Overall, WP = 150-100-100 has a good time performance for a high power consumption WP alternative.

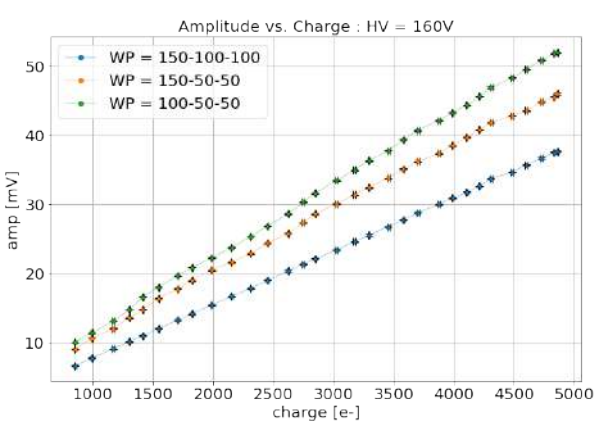

(a) Amp vs. charge

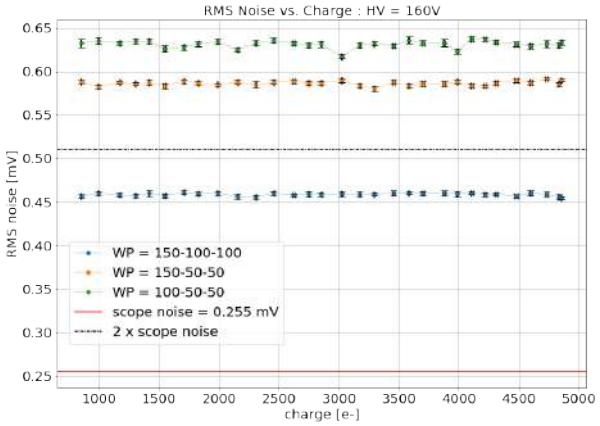

(b) Noise RMS vs. charge

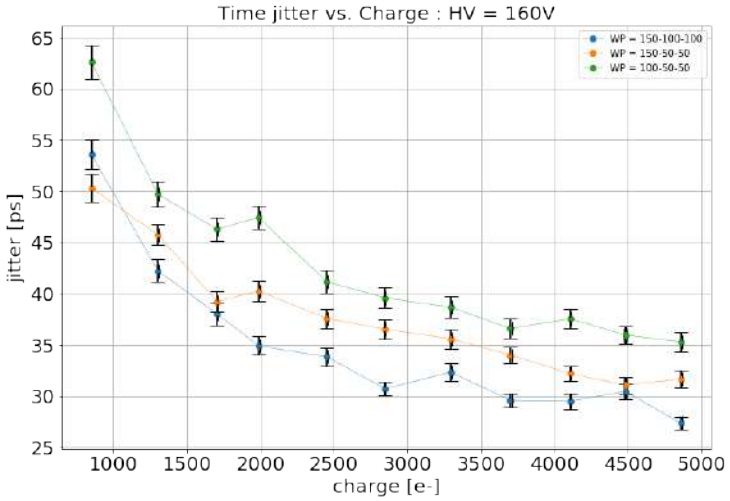

(c) Time jitter vs. charge

Figure 4.9: Measurements of: (a) amplitude vs. charge, (b) RMS noise vs. charge, and (c) *toa* jitter vs. charge for working points WP=150-100-100, WP=150-50-50 and WP=100-50-50, at a HV= −160V.

Board 114 Laser Time Resolution Summary Table, HV = −160V Working points WP=150-100-100, WP=150-50-50, WP=100-50-50, Vcc=1.7V						
Preamp [μA]	Feedback [DAC]	Driver [DAC]	Intensity [%]	Amplitude [mV]	charge [e-]	Time resolution Toa jitter [ps]
150	100	100	100	37.67 ± 0.08	4859.82 ± 7.37	27.36 ± 0.63
150	100	100	67	23.38 ± 0.07	3024.43 ± 5.65	31.52 ± 0.76
150	100	100	34	6.62 ± 0.05	850.82 ± 3.17	53.59 ± 1.43
150	50	50	100	46.03 ± 0.08	4859.82 ± 7.37	31.66 ± 0.88
150	50	50	67	30.06 ± 0.05	3024.43 ± 5.65	36.05 ± 0.97
150	50	50	34	9.03 ± 0.04	850.82 ± 3.17	50.31 ± 1.37
100	50	50	100	51.96 ± 0.08	4859.82 ± 7.37	35.30 ± 0.95
100	50	50	67	33.44 ± 0.05	3024.43 ± 5.65	37.58 ± 1.02
100	50	50	34	10.01 ± 0.04	850.82 ± 3.17	62.59 ± 1.67

Table 4.3: Results of time jitter for WP=150-100-100, WP=150-50-50 y WP=100-50-50.

WPs with medium power consumption

The working points analyzed so far have a fairly high preamp current, which implies a necessarily high power consumption. To consider other more economical working points in terms of power consumption, measurements were made with lower values of preamp current.

We know that the results of time resolution are correlated with the power consumption of the chip, so a lower power consumption implies higher time jitter, which is exactly what is shown in Figure 4.10 and Table 4.4. The reader can concur that even though the results are slightly higher in time resolution, they are still below 40ps for the highest charge production, which means that they are still in the order of magnitude of an ultra-fast timing detector.

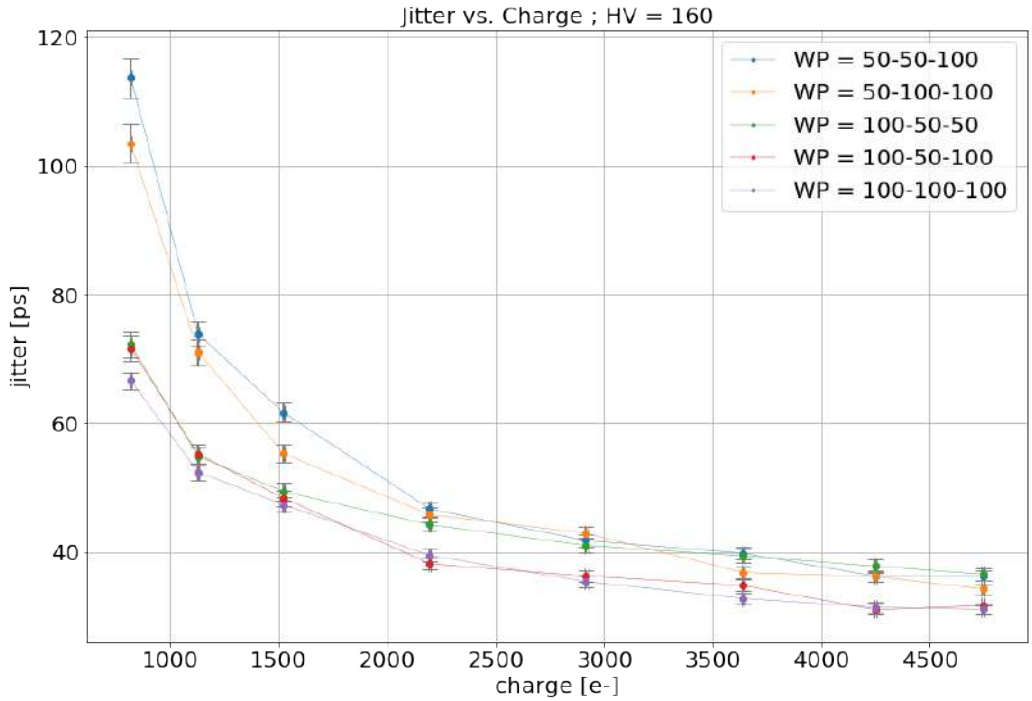

Figure 4.10: *Toa* jitter at HV = −160V for five different working points in the medium power consumption range.

Board 114 Laser Time Resolution Summary Table: Medium Power Consumption HV = −160V C = 100nF, Vcc = 1.7V						
Preamp [μA]	Feedback [DAC]	Driver [DAC]	Intensity [%]	Amplitude [mV]	charge [e-]	Time resolution Toa jitter [ps]
50	50	10	100	29.18 ± 0.058	4746.53 ± 7.68	36.30 ± 0.79
50	50	100	67	17.88 ± 0.047	2915.24 ± 7.92	41.82 ± 0.98
50	50	100	34	4.34 ± 0.027	819.52 ± 3.47	113.72 ± 3.05
50	100	100	100	27.94 ± 0.049	4746.53 ± 7.68	34.28 ± 0.85
50	100	100	67	14.88 ± 0.04	2915.24 ± 7.92	42.95 ± 1.18
50	100	100	34	4.16 ± 0.02	819.52 ± 3.47	103.48 ± 3.05
100	50	50	100	41.68 ± 0.08	4746.53 ± 7.68	36.58 ± 0.96
100	50	50	67	25.69 ± 0.05	2915.24 ± 7.92	41.05 ± 1.08
100	50	50	34	7.21 ± 0.04	819.52 ± 3.47	72.23 ± 1.94
100	50	100	100	34.58 ± 0.09	4746.53 ± 7.68	31.72 ± 0.12
100	50	100	67	21.29 ± 0.07	2915.24 ± 7.92	36.28 ± 0.94
100	50	100	34	5.17 ± 0.05	819.52 ± 3.47	71.68 ± 2.04
100	100	100	100	29.74 ± 0.06	4746.53 ± 7.68	31.13 ± 0.78
100	100	100	67	17.79 ± 0.06	2915.24 ± 7.92	35.41 ± 0.85
100	100	100	34	4.50 ± 0.02	819.52 ± 3.47	66.64 ± 1.26

Table 4.4: Results of time resolution for medium power consumption working points at HV = −160V.

WPs with low power consumption

Finally, to complete these series of measurements, the results for low power consumption WPs shall be shown. As it is already known, there is a correlation between power consumption and time resolution. Thus, for the selected working points, when preamp currents are increased, time jitter lowers.

The results are plotted in Figure 4.11, and a summary is presented in Table 4.6. These working points have achieved results between 200ps and 50ps for charges of $1500e^-$ up to $4000e^-$ with a HV of −140V applied, which is promising considering that for particle detectors that would need hundreds or thousand of detectors, power consumption budget needs to be as low as possible.

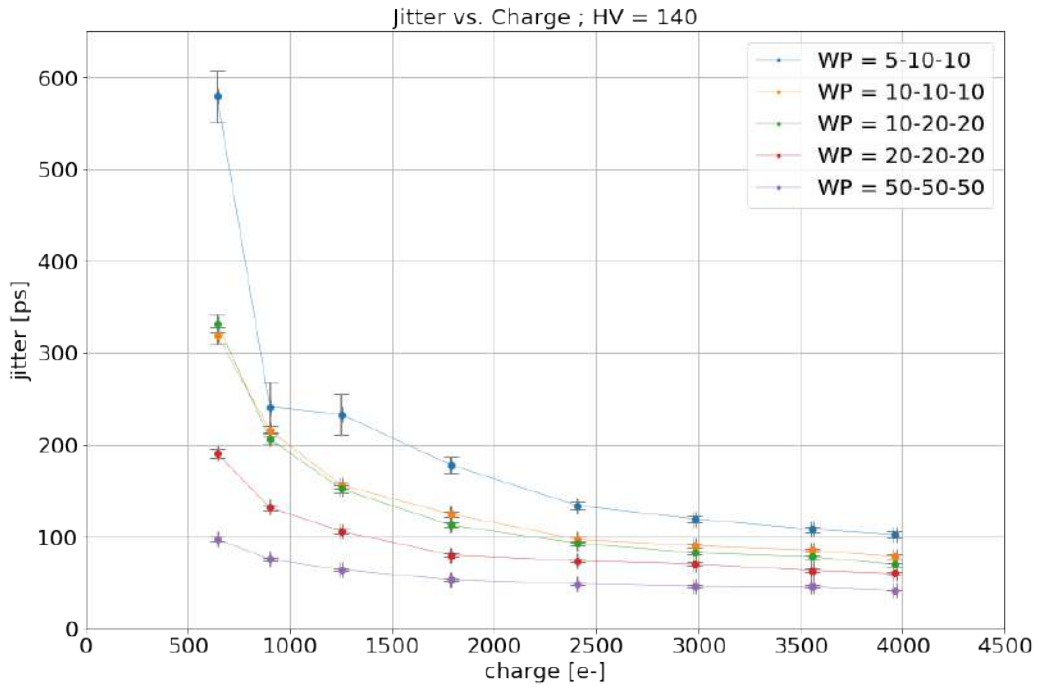

Figure 4.11: *Toa* jitter vs. charge at HV = −140V for five different working points in the low power consumption range.

Board 114 Laser Time Resolution Summary Table: Low Power Consumption HV = −140V, C = 100nF, Vcc = 1.7V						
Preamp [μA]	Feedback [DAC]	Driver [DAC]	Intensity [%]	Amplitude [mV]	charge [e-]	Time resolution Toa jitter [ps]
5	10	10	100	17.50 ± 0.05	3962.56 ± 5.80	102.64 ± 3.04
5	10	10	67	11.75 ± 0.05	2408.13 ± 5.53	134.08 ± 4.26
5	10	10	34	4.44 ± 0.04	640.96 ± 4.75	579.28 ± 28.23
10	10	10	100	27.08± 0.05	3962.56 ± 5.80	78.66 ± 2.21
10	10	10	67	19.00 ± 0.05	2408.13 ± 5.53	97.22 ± 2.51
10	10	10	34	6.70 ± 0.04	640.96 ± 4.75	319.31 ± 9.38
10	20	20	100	25.18 ± 0.05	3962.56 ± 5.80	70.14 ± 1.68
10	20	20	67	16.79 ± 0.05	2408.13 ± 5.53	93.02 ± 2.46
10	20	20	34	5.18 ± 0.05	640.96 ± 4.75	332.62 ± 10.02
20	20	20	100	35.15 ± 0.054	3962.56 ± 5.80	60.16 ± 1.43
20	20	20	67	23.03 ± 0.05	2408.13 ± 5.53	74.07 ± 1.56
20	20	20	34	7.18 ± 0.05	640.96 ± 4.75	190.94 ± 4.33
50	50	50	100	38.56 ± 0.05	3962.56 ± 5.80	42.10 ± 0.96
50	50	50	67	23.66 ± 0.05	2408.13 ± 5.53	49.09 ± 1.27
50	50	50	34	7.00 ± 0.04	640.96 ± 4.75	97.51 ± 2.29

Table 4.5: Results of time resolution for low power consumption working points and HV= −140V.

4.1.2 Board 6439

WP = 150-100-100

This section shows the results obtained by characterizing Board 6439 with gain layer and the highest dose of doping.

The working point to be considered was WP = 150-100-100, Vcc = 1.7V. A scan on laser intensities was carried out from 100 % to 66 % with a step size of 2.2 %, maintaining the values of HV at −80V, −100V, −120V.

A HV scan was also performed from −80V to −135V in steps of 5V at constant laser intensity of 100 %. Amplitude, noise and *toa* jitter analysis was performed.

Figure 4.12 shows the amplitude relation with the HV and we notice that if we fit with a crescent soft curve, the only point that is outside of such behaviour is at HV = −80V. This suggests that at this HV, the lacking amplifier performance of the chip is most probably caused by a not completely depleted gain region. However, already at −85V and until −135V the amplitude has a consistent behaviour, so the borderline of full depletion should be very close to −80V. We can see in Figure 4.13(a) that the relation of the amplitude with

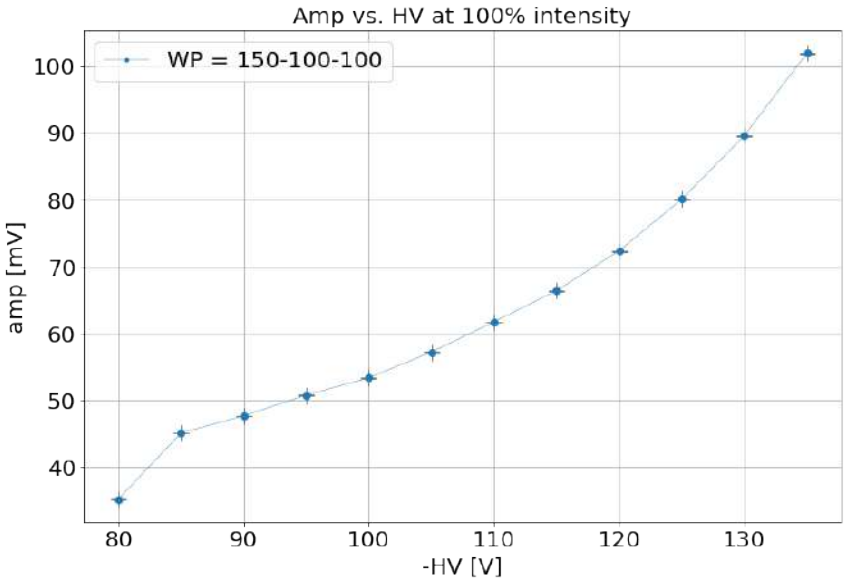

Figure 4.12: Amp vs. HV, WP=150-100-100, maximum intensity.

respect to the laser intensity is well behaved and similar to the one observed for Board

114. In practical terms, we can approximate the relation to a linear function, although for this board, such approximation would imply bigger error. Note that the intensity scan and the HV scan noise measurements shown in Figure 4.13(b) were done at different times and they showed discrepancies in the intrinsic scope noise, which was 0.267mV and 0.365mV respectively. In any case, we see that the noise is neither a function of the HV nor the intensity, and the ratio of RMS noise/scope noise is consistently between 1.5 and 2.

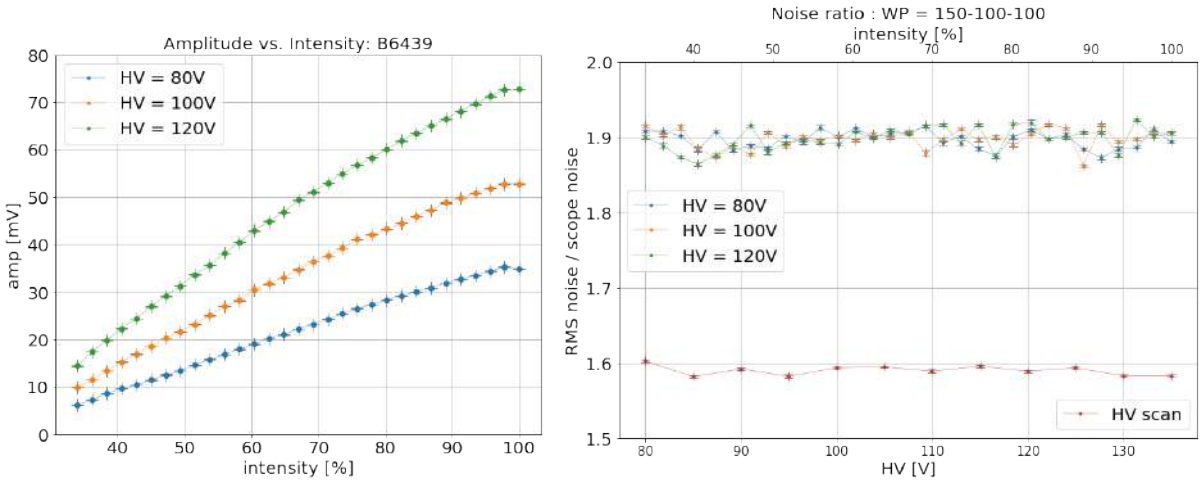

(a) Amp vs. intensity for HV = −80V, −100V, and −120V.

(b) On top, noise RMS/scope noise as a function of intensity (top scale). On bottom, same variable as a function of HV (bottom scale).

Figure 4.13: Analysis of amplitude and noise ratio for WP=150-100-100 at HV = −80V, −100V, and −120V.

The time resolution results obtained for the working point WP = 150-100-100 on the Board 6439 are summarized in Table 4.6: If we compare the results of amplitude of Board 6439 with respect to Board 114 on the previous section, under the same conditions and for the same working point WP=150-100-100, we find that the amplitude for Board 6439 is between 226%-244% of the amplitude of Board 114 with a HV = −100V and 260%-299% with a HV = −120V.

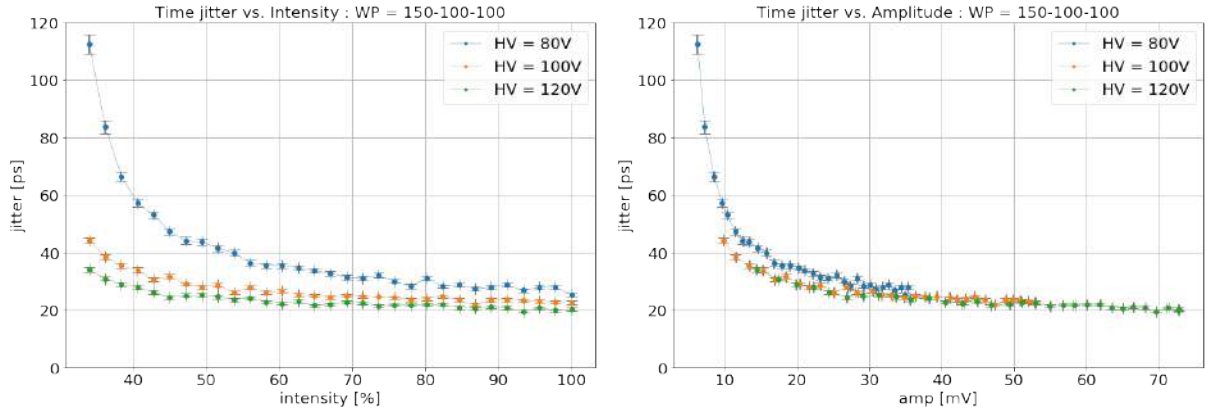

(a) *Toa* jitter vs. intensity

(b) *Toa* jitter vs. *amp*

Figure 4.14: *Toa* jitter vs. intensity for WP=150-100-100 and HV = −80V, −100V, −120V.

Board 6439 Laser Time Resolution Summary Table WP=150-100-100			
−HV [V]	Intensity [%]	Amplitude [mV]	Time resolution Toa jitter [ps]
80	100	34.92 ± 0.04	25.39 ± 0.55
80	67	22.21 ± 0.04	32.79 ± 0.75
80	34	6.27 ± 0.03	112.48 ± 3.25
100	100	52.81 ± 0.07	22.70 ± 0.59
100	67	34.78 ± 0.09	24.53 ± 0.57
100	34	9.86 ± 0.04	44.25 ± 1.02
120	100	72.78 ± 0.08	20.36 ± 0.53
120	67	49.37± 0.07	22.16 ± 0.53
120	34	14.43 ± 0.05	34.07 ± 0.86

Table 4.6: Results of time resolution for Board 6439, WP=150-100-100.

WP = 150-75-255

Finally, seeking to improve the time resolution result obtained and taking it below 10ps, the working point WP = 150-75-255, Vcc = 1.7V was selected. The oscilloscope used was changed to a Lecroy Oscilloscope with bandwidth = 8GHz, sampling rate = 40G·samples/sec, and the C = 100nF external capacitor was kept connected. A scan was made now in the values of HV = −80V, −90V, −100V, −110V, −120V, −130V. Likewise, the results of the amplitude, noise and *toa* jitter analysis were obtained.

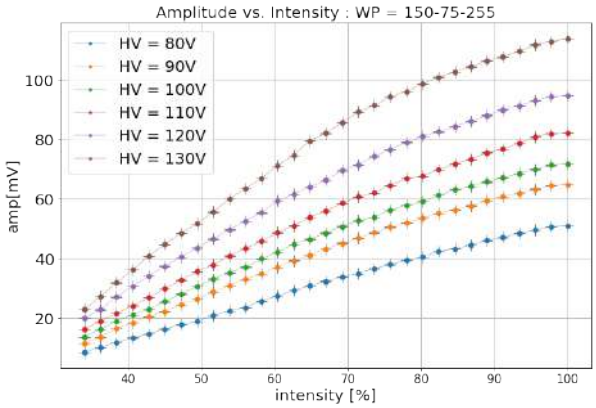

(a) Amp vs. intensity

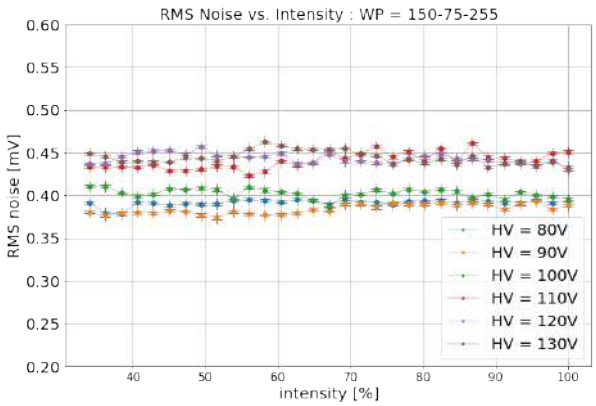

(b) Noise RMS vs. intensity

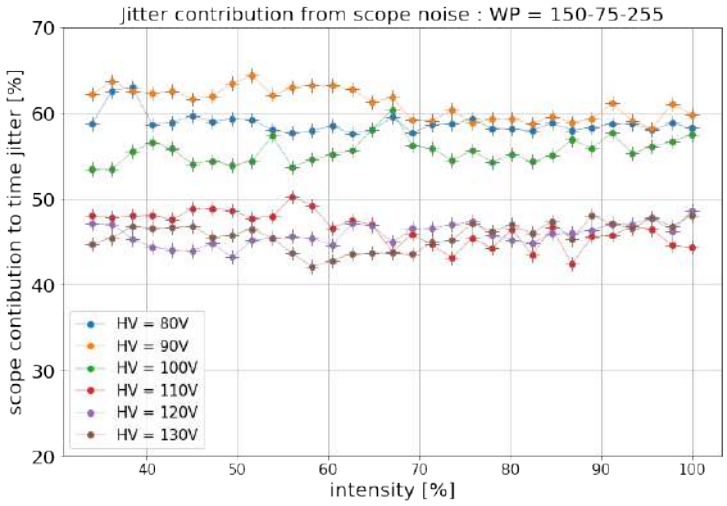

(c) Scope contribution to *toa* jitter vs. intensity

Figure 4.15: Amplitude and noise analysis for WP=150-75-255.

The results obtained with the WP=150-75-255 configuration are, so far, the best results considering all the boards characterized in all the reported working points. In Figure 4.15, we have the complete analysis for the behaviour of the amplitude vs. intensity. The linear approximation weakens with higher voltages, but from Figure 4.15(a) we can claim that it remains valid for intensities below 70%. Figure 4.15(b) and 4.15(c) show the RMS noise and the intrinsic noise contribution to the time jitter. It is important to remember that, whilst high values of the signal-to-noise ratio are required, RMS noise that approximates the oscilloscope's intrinsic noise derives in a higher contribution of the oscilloscope to the time jitter.

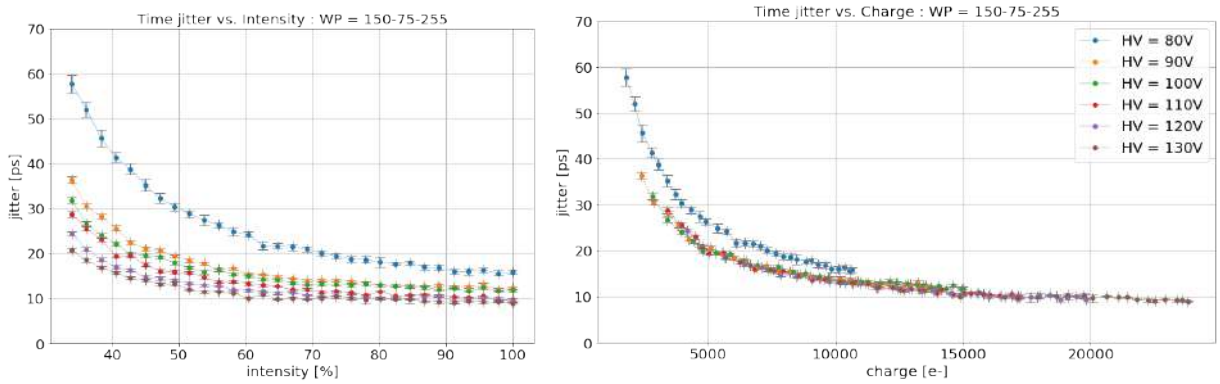

(a) *Toa* jitter vs. intensity

(b) *Toa* jitter vs. charge

Figure 4.16: *Toa* jitter vs. intensity(left) and charge(right), WP=150-75-255 for HV = −80V, −90V, −100V, −110V, −120V, −130V.

In Figure 4.16, the *toa* jitter is plotted as a funcion of, (a): the intensity, and (b): the charge produced inside the detector. Values below 10ps were obtained for this working point starting from a value of high voltage as low as HV = −110V. The gain observed on the data of this board is considerable in comparison with the boards of the previous batch, including Board 114, which showed virtually no gain.

Table 4.7 summarizes the *toa* jitter results and its corresponding amplitude and intensity of laser. Because charge generation process inside the chips with gain is not yet well defined, charge equivalences are not presented in the table.

Board 6439 Laser Time Resolution Summary Table WP=150-75-255, Vcc = 1.75V			
−HV [V]	Intensity [%]	Amplitude [mV]	Time resolution Toa jitter [ps]
80	100	50.96 ± 0.05	15.93 ± 0.47
80	67	32.33± 0.04	21.47 ± 0.70
80	34	8.45 ± 0.03	57.77 ± 1.98
90	100	64.82 ± 0.05	12.32 ± 0.33
90	67	43.25 ± 0.08	14.50 ± 0.28
90	34	11.43 ± 0.05	36.40 ± 0.72
100	100	71.79± 0.10	11.88 ± 0.25
100	67	48.68± 0.07	13.47 ± 0.32
100	34	13.54 ± 0.04	31.86 ± 0.65
110	100	82.36 ± 0.07	9.83 ± 0.25
110	67	56.00± 0.06	11.96 ± 0.27
110	34	16.25 ± 0.04	28.79 ± 0.60
120	100	94.92 ± 0.06	9.42 ± 0.17
120	67	66.44 ± 0.07	11.34 ± 0.46
120	34	20.03 ± 0.04	24.51 ± 0.46
130	100	114.09 ± 0.08	8.96 ± 0.20
130	67	82.15 ± 0.18	10.17 ± 0.20
130	34	22.83 ± 0.04	20.79± 0.44

Table 4.7: Results of time resolution for Board 6439, WP=150-75-255.

4.2 Comparison between laser and ^{90}Sr results

The results reported below correspond to the time resolution obtained when laser events are used to reproduce the ^{90}Sr spectrum. The method to obtain these results was explained in Section 3.6.

Selection and cut of laser events method

A selection and cut of the laser events method for reproduction of the ^{90}Sr spectrum is used, as explained in Section 3.6. Figure 4.17(a) shows the results of the *toa* jitter as a measure of the time resolution for the WP=150-100-50, considering the high power consumption alternative. Figure 4.17(b) shows the low power consumption alternative WP=7-10-200. Figure 4.18 shows the results of the measurements obtained in 4.17 as well as the ^{90}Sr TOF measurements for the same working point obtained in [32]. In Table 4.8, the compared results from Figure 4.17 are presented numerically. The time resolution of the laser events is better than TOF results by 22-28% for WP=150-100-50, and 25-37% for WP=7-10-200.

The error of the laser measurements with respect to the ^{90}Sr TOF measurements is 36-52% for WP=150-100-50, and 38-44% for WP=7-10-200.

Note that the error of the time resolution of the ^{90}Sr TOF measurements has been fixed to 2.5ps. This can be understood as the systematic error of the experimental setup of the data taking, and more specifically, it can be associated to the incertitude of the LGAD detector time resolution, which was used to calculate the TOF. For more information regarding these measurements, refer to [32].

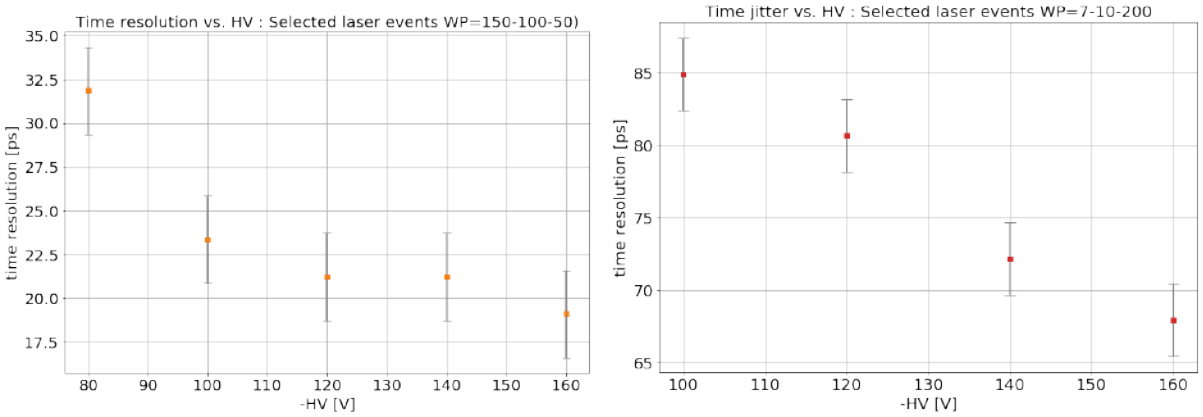

(a) Charge vs. intensity

(b) Noise RMS vs. charge

Figure 4.17: Results of time resolution vs. −HV for (a) WP=150-100-50 and (b) WP=7-10-200.

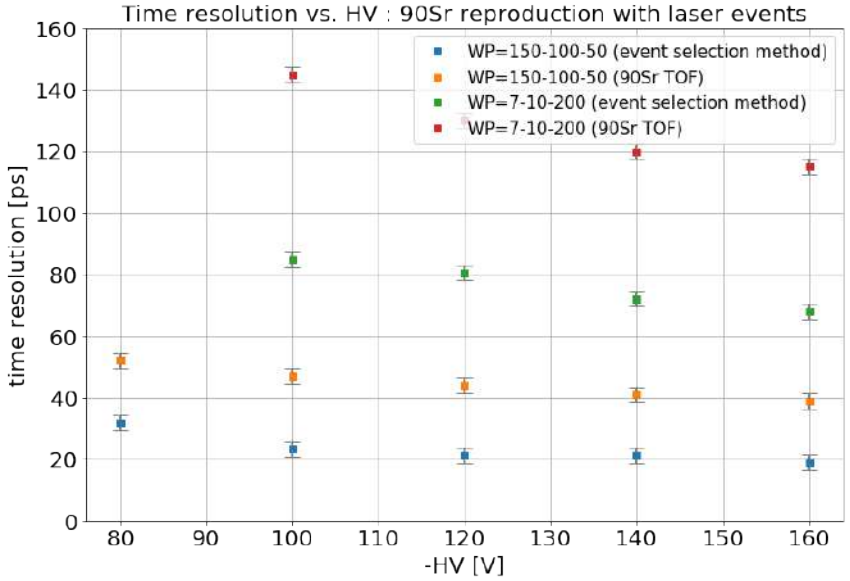

Figure 4.18: Comparison of time resolution results obtained with selection of laser events method vs. TOF results obtained with ^{90}Sr source for WP=150-100-50 and WP=7-10-200.

Laser vs. ^{90}Sr Time Resolution Summary Table Laser event selection, method, Board 114						
Preamp [μA]	Feedback [DAC]	Driver [DAC]	$-$HV [V]	Vcc [V]	Time resolution laser events [ps]	Time resolution ^{90}Sr source [ps]
150	100	50	80	1.8	31.85 $\pm$ 2.5	52 $\pm$ 2.5
150	100	50	100	1.8	23.35 $\pm$ 2.5	47 $\pm$ 2.5
150	100	50	120	1.8	21.23 $\pm$ 2.5	44 $\pm$ 2.5
150	100	50	140	1.8	20.23 $\pm$ 2.5	41 $\pm$ 2.5
150	100	50	160	1.8	19.11 $\pm$ 2.5	39 $\pm$ 2.5
7	10	200	100	2.0	84.93 $\pm$ 2.5	145 $\pm$ 2.5
7	10	200	120	2.0	80.68 $\pm$ 2.5	130 $\pm$ 2.5
7	10	200	140	2.0	72.19 $\pm$ 2.5	120 $\pm$ 2.5
7	10	200	160	2.0	67.94 $\pm$ 2.5	115 $\pm$ 2.5

Table 4.8: Results of time resolution of ^{90}Sr reconstructed spectrum with laser events. Selection and cut of laser events method was used.

CHAPTER 5

Conclusions

Based on the results showed in the previous chapter, it can be said that the main objectives of this work were satisfied. In particular, it was possible to characterize the temporal response of the detector and it was verified that a monolithic silicon detector with SiGe BiCMOS technology without a gain layer can achieve a time resolution below 30ps when configuring the chip in the working points of highest power consumption and the laser source at its highest intensity. For the working points with the lowest power consumption, it was found that the detector achieves a time resolution below 100ps when using the laser source at its highest intensity. This means that this new technology can be an excellent candidate for silicon detectors in HEP experiments or other applications, for example, the PET Scanner in the field of Medical Physics. On the other hand, it was observed that by implementing a gain layer to the original no-gain chip design, the time resolution can reach values below 10ps when configured in the working points of highest power consumption.

Finally, when making a reconstruction of the ^{90}Sr source distribution using the data obtained with the laser, it was found that it is possible to approximate the TOF values with the laser events, however the results differ in a range of 38% to 44%. The best value obtained within this framework was 19ps for the high power consumption working point, and 68ps for the low power consumption operating point, both applying a high voltage of HV$= -160$V. Since these results originate from the events acquired with the laser and not from using a source of MIPs, they must be taken with caution.

A possible explanation to the discrepancy between laser and ^{90}Sr source results could be that the laser measurements only estimate the main source of time jitter contribution to the time resolution, which is time jitter of the amplifier. Considering other sources of time jitter in the analysis will most probably show a closer result of time resolution between laser and ^{90}Sr source. The main consideration is that, even if the distribution in energies of the MIPs of the source has been mimicked with the laser, does not necessarily mean that the waveforms are going to be the same. We have learned that the shape of the waveforms is essential for calculating the time resolution.

In future work, other operating points could be explored, and the specific power consumption determined for each of them. This would be useful to calculate the total power consumption needed to support a specific experiment, such as those at the LHC, or a specific equipment, such as a PET Scanner. This will allow to adapt the conditions to meet a given power consumption budget.

References

[1] ATLAS Collaboration, *Observation of a new particle in the search for the Standard Model Higgs boson with the ATLAS detector at the LHC*, Physics Letters B (2012).

[2] S. Bilenky, *Neutrino oscillations: from an historical perspective to the present status*, Nuclear Physics B (2016).

[3] Y. G. Ma et al, *A brief review of antimatter production*, Frontiers of Physics (2012).

[4] L. Łukasiak & A. Jakubowski, *History of Semiconductors*, Journal of Telecommunications and Information Technology (2010).

[5] The ATLAS Experiment, *ATLAS Fact Sheet*, CERN (2011). `https://cds.cern.ch/record/1457044/files/ATLAS0fact0sheet.pdf`

[6] G. Aad et al, *ATLAS pixel detector electronics and sensors*, IOP Journal of Instrumentation JINST (2008).

[7] P. Riedler, *Overview of Monolithic Silicon Detectors*, CLIC Seminar (2015). `https://indico.cern.ch/event/374145/contributions/1796414/attachments/745477/1022655/CLIC_seminar_032015_priedler.pdf`

[8] J. Adelman et al, *ATLAS FTK Challenge: Simulation of a Billion-fold Hardware Parallelism*, Procedia Computer Science (2015).

[9] E. Cavallaro, *Novel silicon detector technologies for the HL-LHC ATLAS upgrade*, Universitat Autònoma de Barcelona (2018).

[10] The ATLAS TDAQ Collaboration, *The ATLAS Data Acquisition and High Level Trigger system*, IOP Journal of Instrumentation JINST (2012).

[11] M. Benoit et al, *100 ps time resolution with thin silicon pixel detectors and*, IOP Journal of Instrumentation JINST (2016).

[12] D.L. Bailey, *Positron Emission Tomography*, Basic Sciences-Springer (2005).

[13] A.M.J. Paans, *Positron emission tomography*, Department of Nuclear Medicine Molecular Imaging, University Medical Center Groningen (2006).

[14] W. Ni, *The Perils and Pitfalls of Positron Emission Tomography (PET) Quantification Using the Standarized Uptake Value (SUV)*, Department of Electrical Engineering Zaharchuk Group, Radiological Sciences Laboratory (2014).

[15] C. Grupen B. Schwartz, *Particle Detectors*, Cambridge University Press (2008).

[16] L. Paolozzi, *Development of particle detectors and related Front End electronics for sub-nanosecond time measurement in high radiation environment*, Università degli Studi di Roma "Tor Vergata" (2014).

[17] A. Einstein, *On a heuristic point of view concerning the production and transformation of light*, Annalen der Physik 17 (1905).

[18] W. Shockley, *Currents to Conductors Induced by a Moving Point Charge*, Journal of Applied Physics 9, 635 (1938).

[19] S. Ramo, *Currents Induced by Electron Motion*, Proceedings of the I.R.E. (1939).

[20] D. M. Friedl, *The CMS Silicon Strip Tracker and its Electronic Readout*, Vienna University of Technology (2001).

[21] H. Spieler, *Electronics II : Timing Measurements and Signal Digitization*, Lectures on Detector Techniques : Stanford Linear Accelerator Center (1998).

[22] F. Martinelli, *High-Speed Systems for Fast Timing Detectors*, CERN/AQUA Lab, EPFL (2019).

[23] K. Wu et al, *Design of Low Gain Avalanche Detectors (LGAD) with 400 keV ion implantation energy for multiplication layer fabrication*, Nuclear Instruments and Methods in Physics Research Section A (2020). https://www.sciencedirect.com/science/article/abs/pii/S0168900220309554

[24] G. Iacobucci et al, *A 50 ps resolution monolithic active pixel sensor without internal gain in SiGe BiCMOS technology*, IOP Journal of Instrumentation JINST (2019).

[25] L. Paolozzi, *SiGe BiCMOS electronics for ultrafast particle detection*, ACES Workshop (2020). https://indico.cern.ch/event/863071/contributions/3738785/attachments/2044881/3425577/2020_05_26_ACES_Paolozzi_share.pdf

[26] NKT Photonics, *Pilas DX: Picosecond pulsed diode lasers*, Data Sheets: https://www.nktphotonics.com/wp-content/uploads/sites/3/2018/06/als-pilas-dx.pdf?1583329636

[27] Teledyne LeCroy, *WaveRunner 6 Zi Oscilloscopes 200MHz-4GHz*, Data Sheets: https://cdn.teledynelecroy.com/files/pdf/waverunner-6zi-datasheet.pdf

[28] Teledyne LeCroy, *WaveMaster 8 Zi-A Series 4GHz-45GHz Oscilloscope*, Data Sheets: https://docs.rs-online.com/035e/0900766b8127e31c.pdf

[29] Keithley Instruments, *Model 2410 1100V SourceMeter Power Supply*, Data Sheets: https://download.tek.com/manual/2410_902_01B.pdf

[30] TTi Instruments, *QL355TP Power Supply*, Data Sheets: https://www.testequipmenthq.com/datasheets/TTI-QL355P-Datasheet.pdf

[31] ROOT, *ROOT: Data Analysis Framework*, https://root.cern.ch

[32] C. Mileto T. Moretti, *ATTRACT Project - Chip characterization*, Timing detector development meeting UNIGE (2021). https://indico.cern.ch/event/1007970/contributions/4230062/attachments/2188670/3698606/02-11-2021.pdf